Stimulus duration encoding occurs early in the moth olfactory pathway

Tomas Barta[1,2,3*], **Christelle Monsempès**[1], **Elodie Demondion**[1], **Abhishek Chatterjee**[1], **Lubomir Kostal**[2*], **Philippe Lucas**[1*]

***For correspondence:**
tomas.barta@fgu.cas.cz (TB);
kostal@biomed.cas.cz (LK);
philippe.lucas@inrae.fr (PL)

[1]Institute of Ecology and Environmental Sciences of Paris, INRAE, Sorbonne Université, CNRS, IRD, UPEC, Université de Paris, 78000 Versailles, France; [2]Institute of Physiology of the Czech Academy of Sciences, Prague, Czech Republic; [3]Charles University, First Medical Faculty, Prague, Czech Republic

Abstract Flying insects encounter turbulent environments, where chemotaxis along a concentration gradient makes little sense. Detection of the onset and offset of discrete odor pulses is then expected to become crucial for navigation, but it is not well understood how the olfactory system encodes the offset of the odor pulse. Previous works indicated that the duration of a male moth olfactory receptor neuron's (ORN) spike firing response to pheromone stimuli greatly exceeds the pulse duration. However, these works were based on imprecise odor delivery systems. We built an odor delivery system capable of delivering much sharper pheromone stimuli. The stimuli evoked ORN firing responses that faithfully tracked the stimulus duration, provided the stimulus lasted at least 200 ms. A transient inhibition marked the termination of such stimuli. Shorter stimuli produced a firing response exceeding the stimulus duration. The response shapes could be explained by adaptation of the ORN on only two time scales. With simulations, we showed that the observed limits in stimulus offset detection propagate to the antennal lobe and are likely to be behaviorally significant. Our results increase the understanding of the mechanisms necessary for male moths to navigate through pheromone plumes.

Introduction

Flying insects heavily rely on olfactory cues to search for their mating partner, food and oviposition sites. The turbulent airflow breaks the odor signal, e.g., sex pheromone from a female, into pockets containing odor and pockets with clean air. A male moth searching for a mating partner can then encounter pockets with high concentration of pheromone even at large distances from the female (***Jones, 1983***; ***Murlis et al., 2000***; ***Justus et al., 2002***; ***Celani et al., 2014***). The odor plume does not form a continuous gradient pointing to its source and obtaining a reliable concentration average would take too long for flying insects to efficiently track odor plumes. Instead, the insect has to implement different searching strategies, such as an upwind surge during an odor encounter and cast, crosswind flight without progressing upwind, when the odor signal is lost (***Willis and Baker, 1984***; ***Vickers and Baker, 1994***; ***Kennedy, 1983***; ***van Breugel and Dickinson, 2014***; ***Cardé, 2021***). This searching strategy requires the insect to reliably detect the onset and offset of the odor pocket.

The olfactory receptor neurons (ORNs) typically respond to the odor onset by a fast and intense action potential firing activity. On the other hand, ORNs were not always observed to stop rapidly the firing activity after the odor offset. For example, pheromone sensitive ORNs in moths have been considered to terminate their response very slowly (***Kaissling et al., 1989***; ***Jarriault et al., 2010***; ***Grémiaux et al., 2012***; ***Rospars et al., 2014***; ***Tuckman et al., 2021a***,b). The apparent inability to detect the pheromone stimulus offset by moth ORNs is very surprising, given that male moths

are extremely sensitive to the sex pheromone of their conspecific females (***Kaissling and Priesner, 1970***; ***Mayer and Mankin, 1990***; ***Angioy et al., 2003***; ***Kaissling, 2009***), they exhibit a rich and complex repertoire of maneuvers when navigating pheromone plumes (***Willis et al., 2013***; ***Vickers, 2006***; ***Cardé, 2021***), can successfully track female pheromone plumes at large distances (***Cardé and Charlton, 1984***; ***Elkinton et al., 1987***; ***Shorey, 1976***; ***Wall and Perry, 1987***) and their olfactory system has been shown to be very efficient (***Kostal et al., 2008***; ***Levakova et al., 2018***). The most detailed studies that have attempted to link the odor plume structure with orientation behavior in terrestrial animals are from plume tracking behavior of male moths to female sex pheromone. A driving ambition of this long studied model was the use of insect sex pheromones in pest management (***Witzgall et al., 2010***). These studies are also a source for bioinspired navigation models and biohybrid odor-seeking robots (***Ando et al., 2013***; ***Martinez et al., 2014***; ***Anderson et al., 2020***).

It has been suggested that the slow termination of ORN response depends on the physiochemical properties of the odorant molecules and their interaction with the odor delivery device surfaces (***Martelli et al., 2013***). Moth pheromone molecules have a relatively low volatility, as indicated by their low vapor pressure (***Olsson et al., 1983***) and when used as olfactory stimuli they are likely to exhibit slower dynamics, compared to more volatile compounds. Therefore, we investigated if the slow response termination is a physiological property of ORNs and is important for encoding, or if it is an artefact caused by interactions of pheromone molecules with the odor delivery device.

The analysis of the dynamics of odor coding requires either monitoring or controlling the temporal resolution of odor stimuli. Monitoring the odor stimulus can be done with a photo-ionization detector (PID) with high temporal resolution (***Justus et al., 2002***). Unfortunately, common moth pheromones cannot be detected by a PID, because their ionization energies are too high for the PID lamp. Proton transfer reaction-mass spectrometers (PTR-MS) can monitor the dynamic of odor plumes (***Riffell et al., 2014***), including pheromone plumes. However, the sensitivity of PTR-MS remains too low to monitor pheromone stimuli at physiological concentrations. Therefore, we developed a new odor delivery device to better control the stimulus dynamics.

With our new odor delivery system we observed a tri-phasic pattern in the ORN responses from the moth species *Agrotis ipsilon* and *Spodoptera littoralis*, consisting of an excitatory response at the stimulus onset, inhibitory phase at the stimulus offset and a less intense excitatory activity (rebound activity) following the inhibitory phase. This is in contrast to the widely held belief that responses to pheromone in moth ORNs terminate very slowly and is in fact reminiscent of the projection neuron's (PN) response profile. Yet, when ORNs were subjected to short stimuli, the inhibitory phase disappeared and the response consisted of a single long-lasting burst that significantly exceeded the stimulus duration.

The observed qualitative differences in the response, i.e., mono-phasic response to short stimuli and tri-phasic response to long stimuli, point to slow adaptation of the ORNs. In order to asses the slow adaptation process, we had to isolate the ORN processing capabilities from the dynamics of the odor delivery. To this end, we measured the local field potential (LFP) in the sensilla, which is tightly correlated with the depolarizing current entering the ORN. Recording both the LFP and the firing response allows to study independently the transduction processes leading to the generation of the receptor current and how the spike generating mechanism in the soma responds to this current (***Nagel and Wilson, 2011***). We performed an optimization procedure which allowed us to narrow down the adaptation processes to only two time-scales, providing novel insights into the possible mechanisms leading to the adaptation.

Results

New odor delivery device improves the speed of odor onset and offset

A common type of odor delivery device in insect olfactory studies consists of Pasteur pipettes containing a filter paper loaded with one of the odors/doses to test. An electrovalve (EV) redirects an airstream through the pipette, the small tip of which is introduced into a hole on the side of a glass

tube that bathes the insect antenna with a constant humidified and filtered air-stream (***Montagné et al., 2012***). However, the time constants of rising and falling odor concentrations at the onset and offset of the stimulus can be very long, depending on the physicochemical properties of the odorant (***Vetter et al., 2006***; ***Martelli et al., 2013***; ***Gorur-Shandilya et al., 2019***). First, odors are sticky and adsorption / desorption on surfaces contributes to low-pass filtering of the stimulus dynamics as the odors travels along the tube. Next, the temporal structure of the odor stimuli disintegrates within 10–20 mm from the exit of the odor stimulus device when the airflow is no more restrained within a tubing.

We built an odor delivery device in which we ensured that the effects of odor molecules interacting with surfaces have minimal effect on the dynamics of the delivered stimulus. The insect was placed directly in front of an electrovalve controlling the odorant supply (***Figure 1–Figure Supplement 2***). We tested with linalool (due to its low volatility) that the odor delivery device is capable of delivering sharp and short odor pulses (***Figure 1***A). Adding a glass tube between the PID and the electrovalve (15 cm length, 1 cm diameter) resulted in much slower PID responses and short stimuli evoked only very little response (***Figure 1***B).

Using more volatile compounds (linalool, α-pinene) resulted in sharper PID responses (***Figure 1***C). We suspected that the slowdown of the response dynamics with linalool is not a property of the odor delivery device, but of the PID. To verify this, we performed an experiment where we completely cut off the odor delivery device from the PID by inserting a plastic barrier between them during the stimulation. The time course of the PID response offset remained slow (***Figure 1***D). Although the observed PID response offset was slightly faster in the first 500 ms after the stimulus termination in the experiment with using the plastic barrier, after 500 ms the sustained response was identical (***Figure 1***E-J), indicating that the observed slow dynamics of the response and the long lasting response are mostly a property of the PID and not of the odor delivery device. Possibly the odorant molecules adhere to the surface of the PID and thus slow down their onset and offset detection by the PID. Therefore, we conclude that it is risky to use PID signal as a proxy for odor concentration and the physiochemical properties of the used odorant need to be considered.

Moth ORN response shape tracks odor pulse durations

We presented the pheromone sensitive ORNs of *A. ipsilon* with stimuli of different durations (3 ms, 5 ms, 10 ms, 20 ms, 50 ms, 100 ms, 200 ms, 500 ms, 1 s, 2 s, 5 s) of 100 pg dose. The neurons responded by intense firing activity, reaching its peak approximately 20 ms to 50 ms after the stimulus onset, regardless of the stimulus duration. The time course of the response changed qualitatively with the stimulus duration (***Figure 2***A-B). For a stimulus duration below 100 ms the neurons continued firing for around 100 ms after the stimulus offset, while slowly returning to their spontaneous activity (***Figure 2***C-D). For stimuli longer than 200 ms the firing response terminated sharply with the stimulus offset. The firing response was then followed by an inhibitory phase, lasting approximately 300 ms (***Figure 2***E). During the inhibitory phase (interval 100 ms to 400 ms after the firing response termination) the firing activity was significantly suppressed, compared to the activity that followed (rebound phase, measured as the activity in the period 1 s to 3 s after the firing response termination). The rebound activity increases with stimulus duration, making the inhibitory phase more pronounced and indicating that two opposing processes are at play (***Figure 2***F). A mono-phasic response to short stimuli and inhibitory phase after long stimuli were also observed with higher (1 ng) and lower (10 pg) pheromone doses (***Figure 3***A-B). Moreover, in the dose range 10 pg to 1 ng the shape of the firing profile is mostly independent of pheromone concentration (***Figure 3***C), a property that has been illustrated on *Drosophila* ORNs only with highly volatile odors and may help intensity invariant odor identity coding (***Martelli et al., 2013***). We also saw the same response patterns with the ORNs of *S. littoralis* (***Figure 2–Figure Supplement 1***). These results lead us to the conclusion that the previously reported sustained pheromone responses of the moth ORNs are an artefact caused by interactions of the odor molecules with the tubing of the odor delivery device and should not occur in the nature when the moth is flying sufficiently far

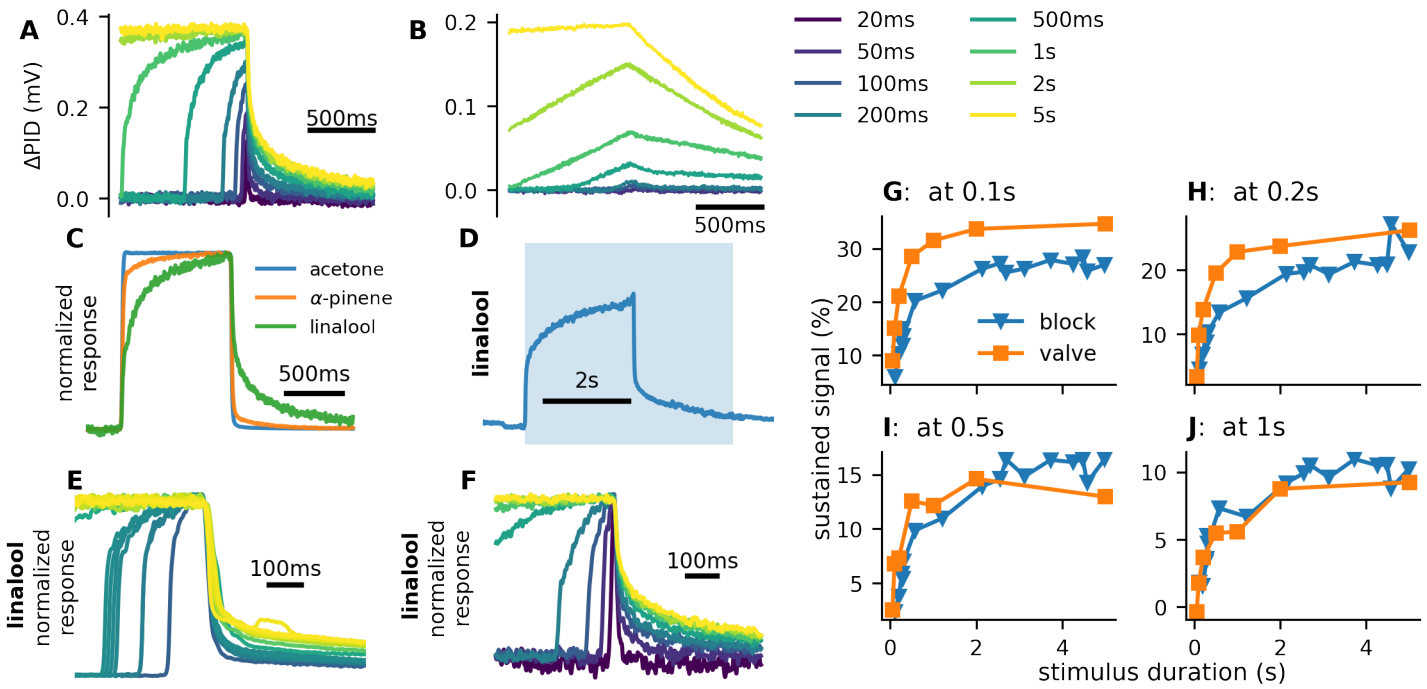

Figure 1. New odor delivery device can deliver square stimuli. A: We verified with PID response to acetone that the odor delivery device is capable of delivering sharp and short odor pulses. On the contrary, adding a 15 cm glass tube after the valve produces responses which are much less sharp and short stimuli (up to 200 ms) evoke very little PID response or no response at all (**B**, we used pure linalool instead of 10% dilution to compensate for airflow mixing in the glass tube). **C:** More volatile compounds produce sharper PID responses. **D:** Shaded area indicates linalool stimulation. Approximately 2.8 s after the stimulus onset a plastic barrier was dropped between the PID and the odor delivery device to prevent any odor molecules from the odor delivery device from reaching the PID. The offset of the PID signal remained slow. **E:** We dropped the barrier at different times after the stimulus onset. The longer the stimulus was, the slower was the PID response offset. We observed the same pattern when we used our odor delivery device to deliver stimuli of different durations (**F**). **G-J:** We compared the value (averaged in a 20 ms window) of the PID at different times after the stimulus offset to its peak value. 0.5 s after the stimulus termination the sustained signal is the same regardless of whether stimulus was terminated regularly (with the electrovalve) or mid-odor delivery with a plastic barrier. This shows that most of the slow dynamics observed with the PID are due to the properties of the PID and not the odor delivery device. All PID responses in the figure were filtered with 49 Hz 2-pole Butterworth lowpass filter to remove noise.

Figure 1–Figure supplement 1. Schematics of the developed odor delivery device.

Figure 1–Figure supplement 2. Testing of equilibration times and source stability.

away from any surfaces that could release previously adsorbed pheromone molecules.

Flying insects use both olfactory and mechanosensory input (from wind speed) to track odor plumes. Antennal lobe neurons integrate both sensory inputs (***Tuckman et al., 2021a***,b). The detection of mechanosensory information in insect antennae is attributed primarily to Johnston's organ and Böhm's bristles in the pedicel of the antenna (***Budick et al., 2007***; ***Sane et al., 2007***; ***Dieudonné et al., 2014***). However, it was recently proposed in the honeybee that mechanosensory signals can also be transduced by olfactory sensilla on the antenna, with changes of sensilla position potentially modulating ORN responses (***Tiraboschi et al., 2021***). To verify that the observed response pattern is not an artefact caused by change in the mechanical pressure at the stimulus offset, we performed recordings where we maintained constant mechanical pressure throughout odor stimuli by delivering odorless air with an electrovalve in opposing phase to the valve controlling the odor delivery. With this setting, we still observed the tri-phasic response pattern (***Figure 2–Figure Supplement 2***).

We still observed some sustained activity long after the stimulus end, with onset after the inhibitory phase. The intensity of the activity increased both with duration and dose of the stimulus (***Figure 3***B) and could last more than 15 min (***Figure 2–Figure Supplement 3***). Our new setup

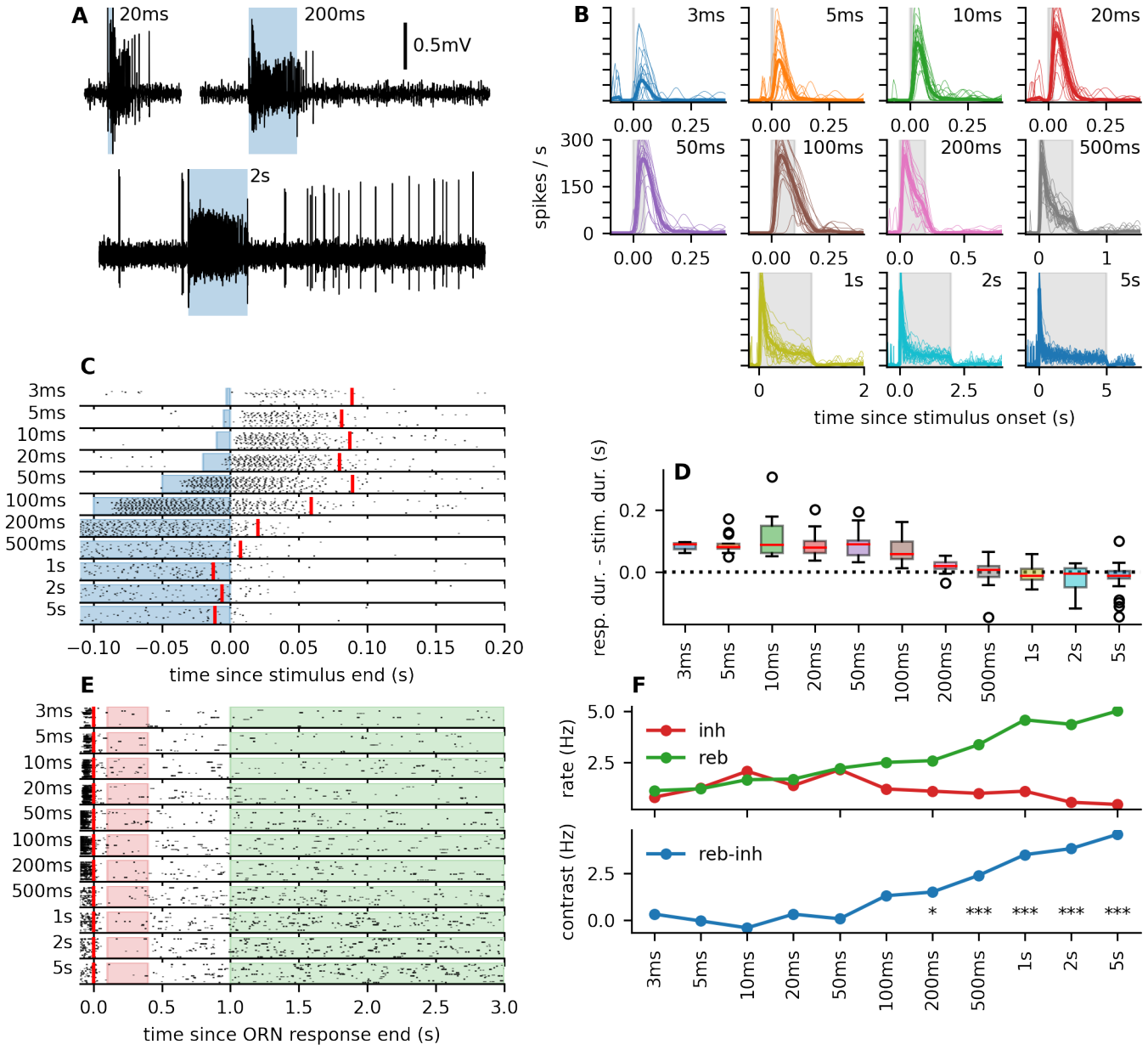

Figure 2. Different stimulus durations produce qualitatively different response terminations. A: Representative voltage traces in response to 20 ms, 200 ms and 2 s stimuli. **B:** Firing responses of the ORNs to stimuli of different durations. Thin lines represent responses of individual neurons, thick line is the average response across all measured neurons (blue area indicates the stimulus period, N=21-23 sensilla). **C:** Raster plots of the spike trains, aligned at the stimulus offset. Responses to stimuli 100 ms and shorter continue after the stimulus offset, while the ends of responses to longer stimuli coincide with the stimulus offset. The red vertical line represents the point in time where 50% of the ORNs' responses finished (see Materials and methods). **D:** Box-plot of how much the response ends exceed the stimulus duration. Color-coded is the stimulus duration, same as in **B**. **E:** Raster plots aligned to the median response end. We compared the firing rates in the red filled area (0.1 s to 0.4 s after the response end) with the firing rates in the green filled area (1 s to 3 s after the response end) to evaluate the contrast between the inhibitory phase and the rebound activity, as shown in **F** (top panel: firing rate during inhibitory / rebound phase, bottom panel: difference between the rebound and inhibitory activity; stars indicate Wilcoxon rank test significance levels).

Figure 2–Figure supplement 1. Response patterns of *Spodoptera littoralis*.

Figure 2–Figure supplement 2. Control experiment with compensating airflow.

Figure 2–Figure supplement 3. Sustained firing activity measured over long periods.

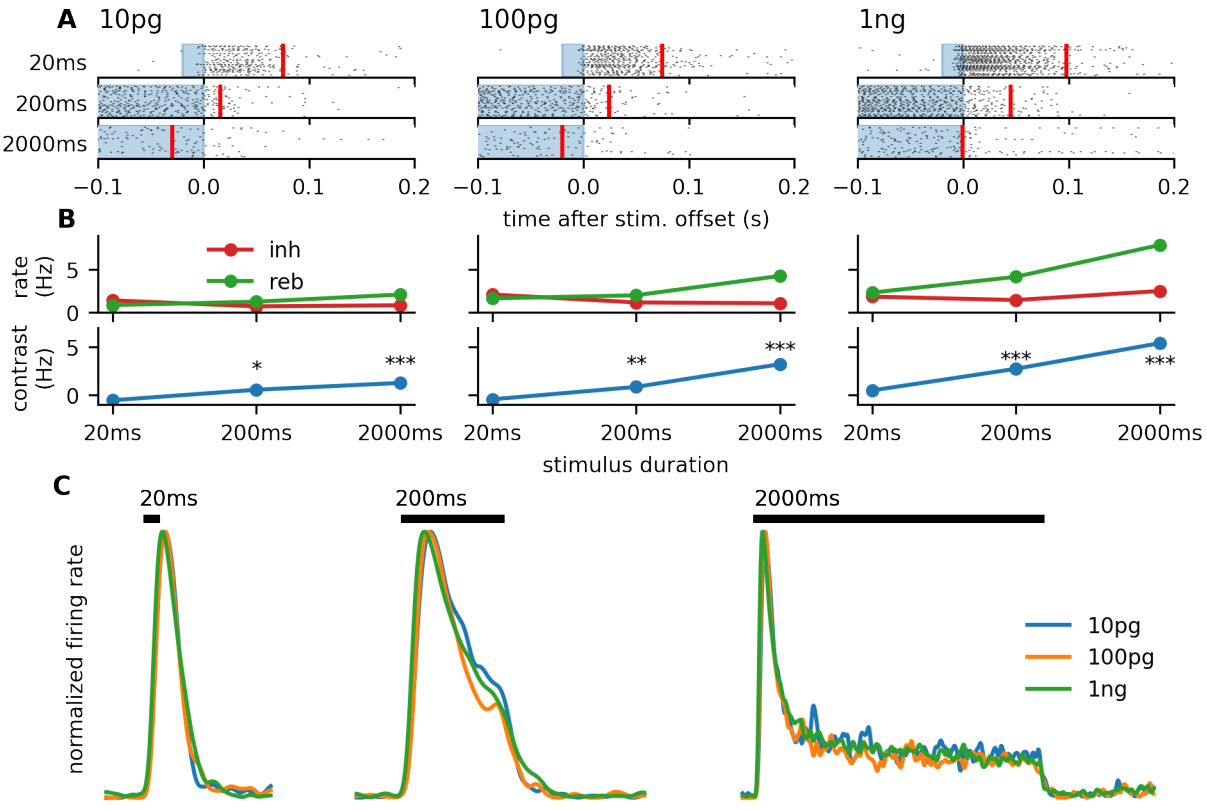

Figure 3. Response properties are maintained with different odor doses. A: Raster plots aligned to the stimulus termination, as in ***Figure 2***C, but with different odorant doses (N=52-57 sensilla). For all doses the spiking response exceeds the short (20 ms) stimulus but terminates rapidly with the longer stimulus (2 s). **B:** The equivalent of ***Figure 2***F for different odorant doses. With all tested doses the neurons exhibited the transient inhibition after the 200 ms and 2 s stimuli. **C:** Firing rate shapes normalized to the peak for different stimulus durations and doses. The general shape is independent of the odorant dose. The black bar indicates the stimulus presence.

strongly reduces the surface where odor molecules can adsorb and then desorb and stimulate the antenna, therefore we conclude that the sustained response has a physiological origin, e.g., pheromone molecules adhering to the sensilla.

Rapid response termination stems from slow spike frequency adaptation

We recorded the LFP simultaneously with the firing activity in response to 20 ms, 200 ms and 2 s stimuli (dose 1 ng). The LFP shape reflects the depolarizing current flowing from the sensillar lymph into the neuron (with a multicompartmental model of the ORN we estimated that the LFP corresponds to the depolarizing current filtered with exponential kernel with 10 ms decay, ***Figure 4–Figure Supplement 1***). After the stimulus onset, the LFP decreases (downward deflection of the LFP signal) due to positive charge flowing from the sensillar lymph into the ORN (exciting the neuron; the amplitude of the LFP deflection is correlated with the peak firing rate; ***Figure 5–Figure Supplement 1***B). The LFP typically exhibits some level of adaptation (upward deflection) followed by an additional downward deflection (***Figure 4***A-D). Shortly after the stimulus offset (within 10 ms) the LFP starts increasing, signifying a decrease in the depolarizing current. After an initial rapid increase, the LFP continues to slowly increase towards the level before the stimulus. This can be either due to a different, slower, signalling pathway or some of the odor molecules can be slowed down by first adhering to the sensilla, before eventually reaching the odor receptors.

The transiency of the firing rate indicates that the firing rate responds to the slope of the depo-

larizing current, as previously observed in *Drosophila* (***Nagel and Wilson, 2011***). However, dependency purely on the LFP and its slope cannot fully explain the shape of the firing rate. Particularly, the average LFP response to 200 ms and 2 s is nearly identical in the period 50 ms before stimulus termination to 100 ms after stimulus termination, but the decreased firing rate indicates that the spike generating mechanism is clearly more adapted after 2 s stimulation (***Figure 5***E). The comparison of LFP to firing rate transformation between the response to 20 ms and the longer stimuli is not straightforward due to the weaker LFP response evoked by the 20 ms stimulus. To facilitate the comparison we shifted the responses by 50 ms, so that the LFP decay after 20 ms stimulation closely follows the LFP decay after 200 ms stimulation, while the firing rate is significantly higher (***Figure 5***A). These results illustrate a clear dependence of the firing activity on the ORN's history.

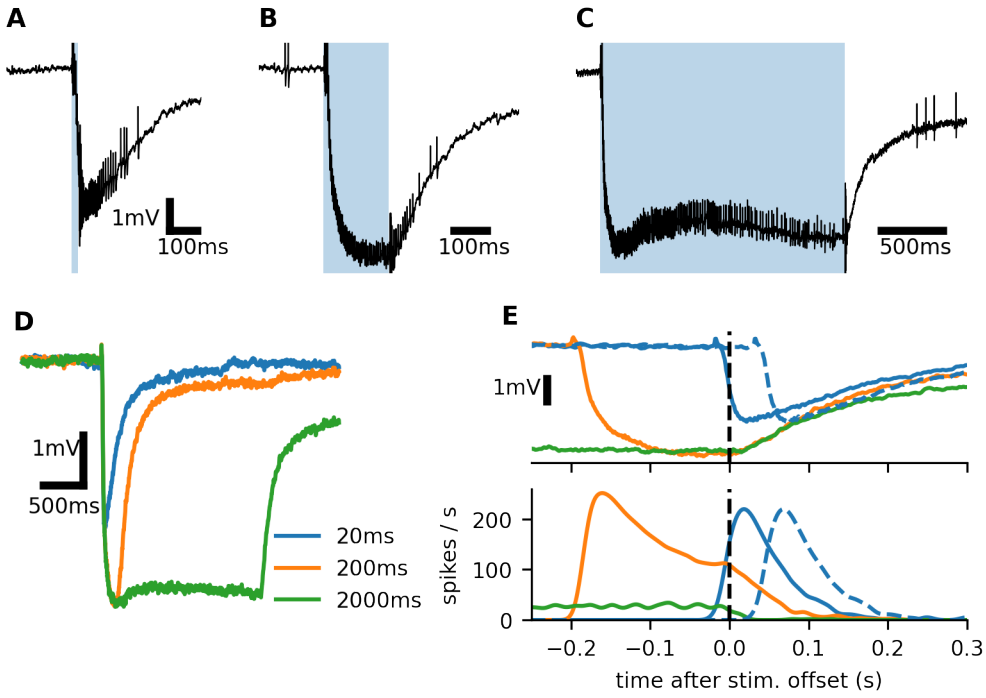

Figure 4. Firing rate depends on the history of the input. A-C: Raw recordings of a single ORN's response to three different stimulus durations. **D:** LFP responses averaged over 26 sensilla. Note that in response to the 2 s stimulus, LFP first increases after the initial decrease, indicating receptor adaptation and after continues to decrease again. This is apparent also in **C**. **E:** LFP (top) and average firing rate (bottom) aligned at the stimulus termination. The LFP after the stimulus offset is identical for the 200 ms and 2 s stimulus, yet their firing rates are dramatically different. The dashed blue lines indicate the response to the 20 ms stimulus, but shifted by 50 ms. Then the LFP time course after the stimulus offset is identical with the 200 ms stimulus, but the firing rates again greatly differ.

Figure 4–Figure supplement 1. Multicompartmental ORN model

Figure 4–Figure supplement 2. Heterogeneity of ORN responses

Figure 4–Figure supplement 3. LFP recordings with TTX

To formalize our claim we used a linear-nonlinear model to predict the firing rate from the LFP (***Figure 5***A):

$$f(t) = N((K_f * \mathrm{LFP})(t)). \tag{1}$$

The linear kernel K_f is composed of multiple gamma distribution-shaped kernels (***Gorur-Shandilya et al., 2017***; ***Jayaram et al., 2022***) and a δ-function, therefore the convolution can be equivalently

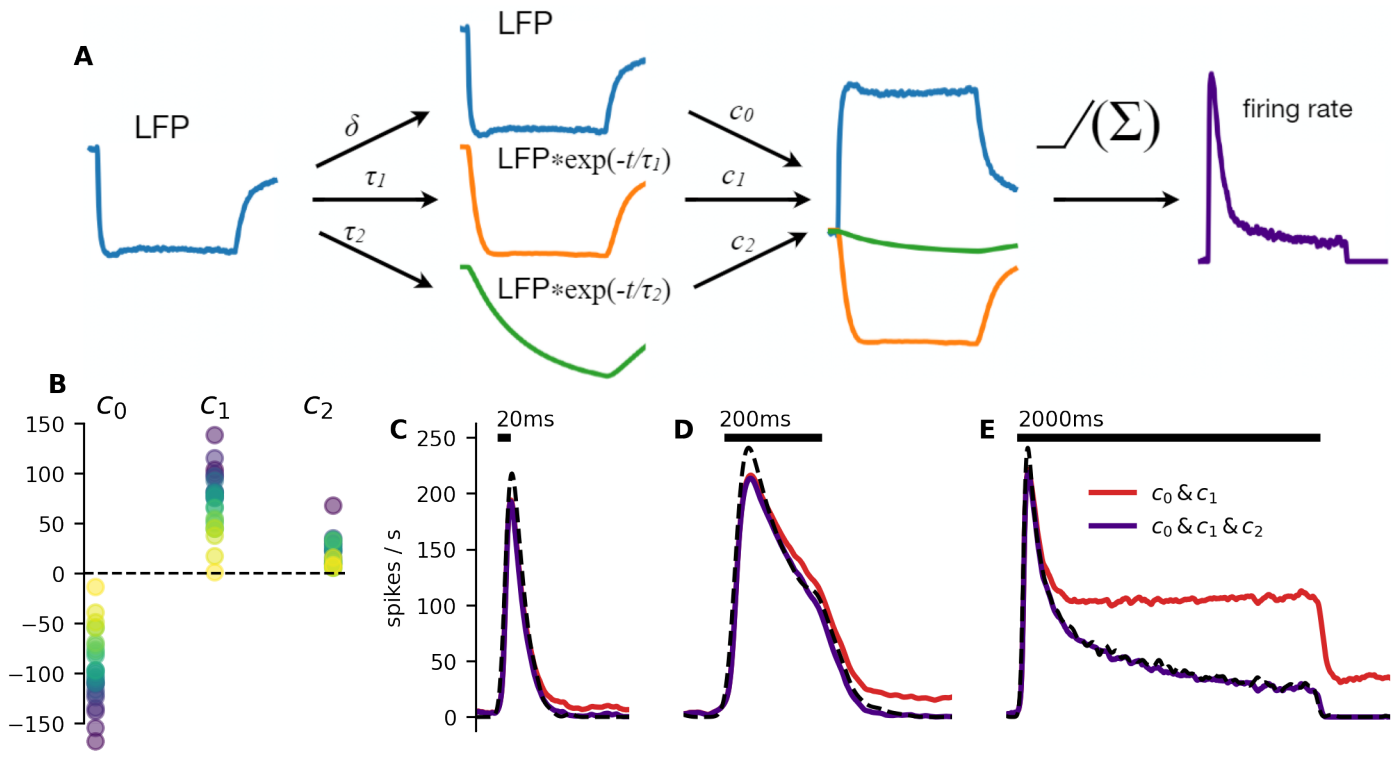

Figure 5. Slow spike-frequency adaptation is necessary to reproduce the ORNs' behavior. A: Illustration of the firing rate prediction process. The LFP was filtered with two different exponential kernels with time constants τ_1 and τ_2. Linear combination of the filtered values and the LFP, followed by a rectifying non-linearity, provides a prediction of the firing rate. This process is equivalent to directly convoluting the LFP with a linear filter composed of two exponential kernels and a δ-function. **B:** Values of the optimal coefficients for all the fitted neurons. Points are color coded by ORNs. **C-E:** Predictions of the firing rate with and without the slow (800 ms) component. Predictions with the full filter closely match the empirical firing rate (dashed black line). The reduced filter predicts well the responses to short stimuli, but fails to predict the response to the 2 s stimulus.

Figure 5–Figure supplement 1. Distributions of filter coefficients and their effect on spike firing properties

Figure 5–Figure supplement 2. Selection of filter time constants

Figure 5–Figure supplement 3. Firing rate prediction using odor transduction model

expressed as

$$K_f * \mathrm{LFP}(t) = c_0 \cdot \mathrm{LFP}(t) + \sum_{k=1}^{n} c_k \cdot (g_k * \mathrm{LFP})(t) \tag{2}$$

$$g_k(t) = \begin{cases} \frac{1}{\Gamma(\alpha_k)\tau_k^{\alpha_k}} t^{\alpha_k - 1} e^{-\frac{t}{\tau_k}} & t \geq 0, \\ 0 & t < 0, \end{cases} \tag{3}$$

where c_k are the linear combination coefficients and τ_k are the time scales $\alpha_k \geq 1$ are the shapes of the gamma distributions. N is a rectifying nonlinearity ($N(x) = \max(0, x)$). Using lasso regression, we found that the firing rate can be reliably predicted from the LFP using only two time scales: 40 ms and 800 ms and the unfiltered LFP (see Materials and methods and ***Figure 5–Figure Supplement 2*** for details, note that the LFP provides a low-pass filtered representation of the depolarizing current).

We fitted the coefficients c_k to a 2 s stimulus (and the preceding 1 s of spontaneous activity) individually to each of 26 different neuron recordings by minimizing the square error between the prediction and the observed firing rate. The average values of the coefficients were $c_0 = -95.4$, $c_1 = 71.7$, $c_2 = 20.4$ (the coefficient distributions and their mutual dependence is shown in ***Figure 5***B

and ***Figure 5–Figure Supplement 1***A). The signs indicate that the neurons respond rapidly to LFP deflection by firing activity ($c_0 < 0$), which is then attenuated by adaptation on two different time scales ($c_k > 0$, $k \geq 1$). The ratio $\frac{c_1+c_2}{c_0}$ is negatively correlated with the steady state-to-peak ratio (***Figure 5–Figure Supplement 1***D). Using only the LFP (indicating the depolarization of the neuron) and two adaptation time scales, we were able to predict very well the ORNs' firing responses (***Figure 5***C-E). Despite being fit only to the 2 s pulse, the predicted firing rate corresponds well even to the responses to the 20 ms and 200 ms pulses, including the firing profile after the stimulus offset, which is different for each pulse duration.

The presented model is the minimal model capable of capturing the shape of the firing response. With $c_2 = 0$ (set after the fitting procedure), the model still predicts well the response to short stimuli (during the short period, the neuron does not become adapted on the slow time scale), however, it does not predict the continued decrease of firing rate during the 2 s long stimulation. If the model is fitted without the slow adaptation, aside from not predicting the time course of the firing rate well, the model does not predict the prolonged responses as well (***Figure 5–Figure Supplement 2***D-F).

We fit the model to each neuron individually, because the pheromone sensitive ORNs of moth exhibit a significant cell-to-cell variability, as analyzed by ***Rospars et al. (2014)***. Apart from the variability in the firing responses, we also observed variability in the LFP shapes (in response to a 2 s stimulus). We verified that the response of a single neuron over multiple trials is stable (exhibits little variability) compared to the measured population ***Figure 4–Figure Supplement 2***.

It is also possible to obtain a full odor-to-firing-rate model. We used a simple transduction model to predict the LFP from the odor concentration (***Nagel and Wilson, 2011***):

$$\mathrm{R} \underset{s_b}{\overset{[\mathrm{O}]k_b s_b}{\rightleftarrows}} \mathrm{OR} \underset{s_a}{\overset{k_a s_a}{\rightleftarrows}} \mathrm{OR}^*, \tag{4}$$

$$\mathrm{LFP} = \mathrm{OR}^* * g_{\mathrm{LFP}}, \tag{5}$$

where R are the unbound receptors, OR are bound, but not activated receptors and OR^* are bound activated receptors, [O] is the odorant concentration, s_a and s_b are the unbinding and deactivation rates and k_a and k_b set the ratio between activation/deactivation and binding/unbinding rates and g_{LFP} is an exponential kernel with 10 ms decay (as estimated from our multicompartmental model; ***Figure 4–Figure Supplement 1***B-C). Because the spontaneous activity of moth ORNs is very low ((0.34±0.03) Hz in *A. ipsilon* ***Jarriault et al., 2010***; 0.5 Hz to 0.8 Hz in *S. littoralis* ***Pézier et al., 2007***; see also ***Figure 2–Figure Supplement 3***), we neglected the activation of unbound receptors. The model predicts well the time course of the firing rate during stimulation and the firing rate offset (***Figure 5–Figure Supplement 3***).

We hypothesized that the adaptation could be facilitated by hyperpolarizing Ca^{2+}-gated K^+ currents in the soma (***Zufall et al., 1991***; ***Lucas and Shimahara, 2002***; ***Pézier et al., 2007***). We illustrated on a multicompartmental model that such hyperpolarizing currents can affect the LFP by further decreasing it (***Figure 4–Figure Supplement 1***D-G) and could thus account for the second downward deflection of LFP during 2 s stimulation. In such case, the second downward deflection could be removed by abolishing the spiking activity and thus also the Ca^{2+} influx due to action potentials. To test this hypothesis, we recorded the LFP after injecting the Na^+ channel antagonist tetrodotoxin (TTX, 50 µM) into the antenna. The TTX injections abolished the spiking activity, however the secondary deflection of the LFP remained (***Figure 4–Figure Supplement 3***). Therefore we conclude that the secondary deflection is not caused by hyperpolarizing currents in the soma triggered by Ca^{2+} influx during action potentials.

Prolonged response to short stimuli is maintained by the antennal lobe

ORNs project their axons to the antennal lobe (AL) onto projection neurons (PNs) and local neurons (LNs). All ORNs expressing the same odorant receptor project their axons to the same glomerulus harboring the dendrites of PNs and LNs (***Kay and Stopfer, 2006***; ***Wilson, 2013***). PNs create excitatory

connections with other PNs and LNs provide an inhibitory feedback both to PNs and LNs. PNs then project their axons to higher brain centers. Therefore, understanding how the PNs reshape the firing response is essential for understanding the implications for behavior of the insect. Even though the observation of the inhibitory phase in moth ORNs is novel, previous studies observed the inhibitory phase in PNs, despite using the classical odor delivery device with Pasteur pipette (***Jarriault et al., 2010***; ***Martinez et al., 2013***). Moreover, PNs are sensitive to the slope of ORN firing rate (***Kim et al., 2015***), which can explain their transient responses. These results suggest that although ORNs are not obviously encoding the stimulus duration of short stimuli (***Figure 2***), the ORN responses could be processed by the AL to provide a more accurate representation of the stimulus duration.

We used the ORN firing rates as an input to an antennal lobe model (***Tuckman et al., 2021a***,b; see Materials and methods for details). We modelled a single glomerulus containing 10 PNs and 6 LNs. PNs create random excitatory connections to PNs and LNs withing the glomerulus and LNs create random inhibitory connection to PNs and other LNs (***Figure 6***A). The PNs are equipped with small conductance Ca^{2+}-activated K^{+} channels (SK channels) which together with the inhibitory input facilitate spike frequency adaptation and make the PNs sensitive to the slope of the ORN input, as also observed with the *Drosophila* PNs (***Kim et al., 2015***). PNs then exhibit a transient inhibition at the end of the stimulus, even if no transient inhibition is observed in the ORN response, in accordance with ***Jarriault et al.*** (***2010***) (***Figure 6***B). However, the response to short stimuli still significantly exceeds the stimulus duration (***Figure 6***C) and the firing profile shape with this model does not differ greatly from the firing profile shape of ORNs (***Figure 6***D). Therefore, we expect that the encoding of duration is not significantly altered by the antennal lobe and thus the longer responses to short stimuli likely propagate further and affect behavioral responses.

Although PNs can exhibit the inhibitory phase even when there is no inhibitory phase in the ORN response, their precision of stimulus duration encoding is improved by the observed dynamics in ORNs. To illustrate this, we made the ORN response less sharp by convolving it with an exponential kernel with 100 ms mean. The smoothed ORN firing profile then did not show any inhibitory phase, but the inhibitory phase was clear in the PN responses. However, the onset of the inhibitory phase did not mark the offset of the stimulus, unlike in the case of the unmodified ORN firing profile (***Figure 6–Figure Supplement 1***).

Discussion

Tri-phasic response of moth ORNs

We found qualitative differences between the responses to short (<200 ms) and long (>200 ms) stimuli. While the spiking response to a short stimulus exceeds the stimulus duration, spiking response to a long stimulus ends with the stimulus. The response to long stimuli marks precisely the stimulus offset with an inhibitory phase. The inhibitory phase was followed by rebound activity. The intensity of the rebound activity increased both with stimulus duration and odor dose.

The observed firing pattern is reminiscent of the pattern observed previously in PNs. Our results therefore show that encoding of temporal structure of the plume happens already at the level of ORNs and not only at the level of PNs, as previously thought (***Jarriault et al., 2010***; ***Rospars et al., 2014***; ***Tuckman et al., 2021b***,a). Moreover, we showed with a simulation that the precise encoding of temporal structure by ORNs also improves the encoding by the PNs, compared to ORN responses with slow offset.

Inhibitory phase marking the end of stimulus has also been observed with various receptor-odor combinations in *Drosophila* (***Nagel and Wilson, 2011***; ***Martelli et al., 2013***; ***Kim et al., 2011***, ***2015***). Moreover, we observed independence of the firing response shape on the odor dose, also previously reported in *Drosophila* with volatile odors. The newly observed similarities between *Drosophila* and moth ORNs unite the research in these different species.

The inhibitory phase was followed by a sustained increase in the firing activity long after the

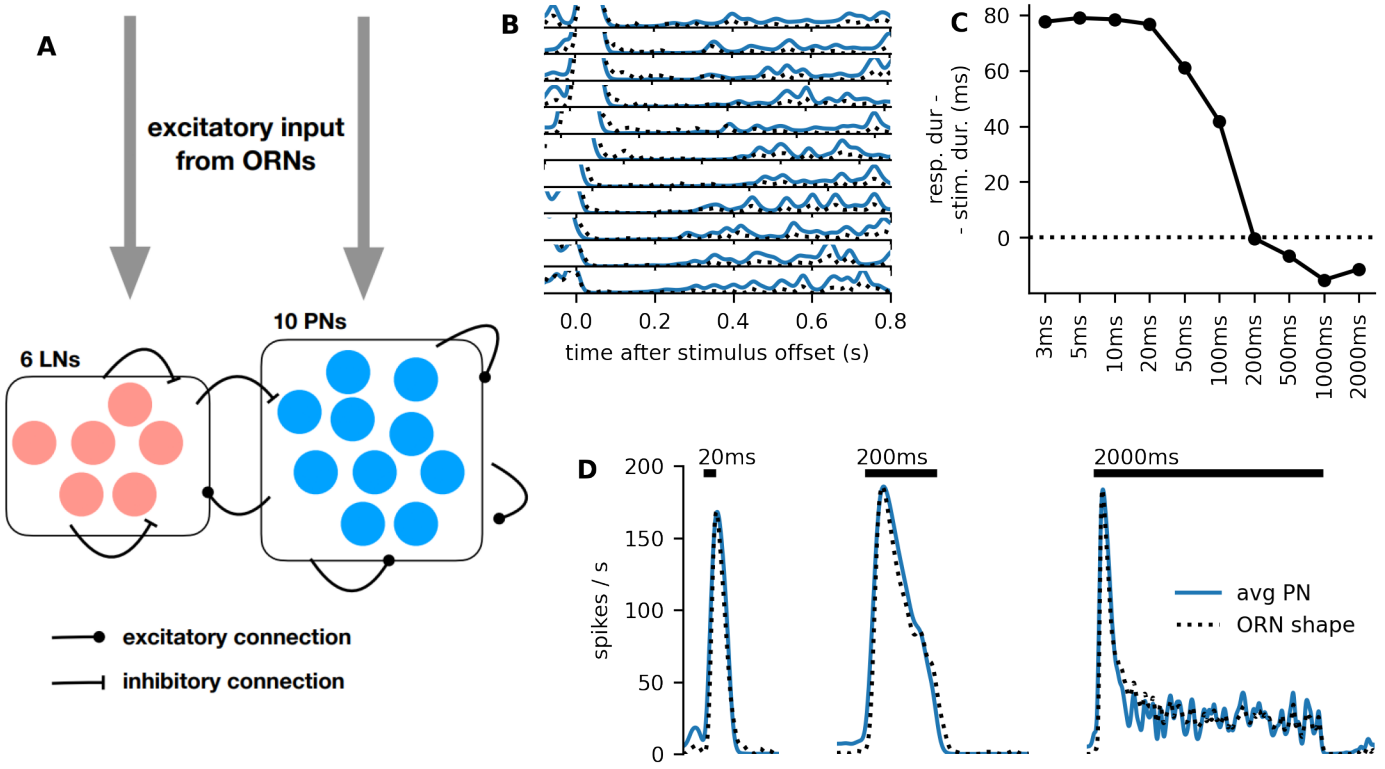

Figure 6. Modelling the antennal lobe. A: Illustration of the used model. **B:** The response end is clearly marked by an inhibitory phase, regardless of the stimulus duration (increasing from top to bottom, 3 ms to 5 s). The y-axis ranges from 0 Hz to 20 Hz. **C:** Although the inhibitory phase clearly marks the response end, the spiking response duration still exceeds significantly the stimulus duration for stimuli shorter than 200 ms. **D:** Average firing rates of the PNs in response to stimuli of different durations. Dotted ORN firing rates were used as an input. Note that the ORN input firing rate is not to scale and is normalized to the peak of the PN firing rate for shape comparison.

Figure 6–Figure supplement 1. PNs do not track odor pulse durations if ORN response is smooth

stimulus termination and also a sustained LFP below the pre-stimulus level, indicating that the sustained firing activity is due to sustained activity of the receptors. With classical odor delivery devices with a Pasteur pipette, such sustained activity could be explained by a slow release of pheromone molecules after closing the valve that controls the stimulus. However, in our experiments, we strongly reduced the possibility of any pheromone molecules adhering to the odor delivery device. The sustained activity could be caused instead by odor molecules adhering to the sensilla and / or it could represent an elevated probability of spontaneous OR-Orco channel opening after prolonged ligand-receptor interaction.

Regardless of the exact mechanism leading to the sustained activity, ORNs seem to remain slightly depolarized long after the stimulus termination and the their detection threshold is thus decreased. It is possible that ORNs evolved to have a very low spontaneous activity prior to any stimulation and after sufficient pheromone exposure the activity is increased in order to decrease the detection threshold and ORNs should respond with higher intensity following a previous stimulus.

Sensitization of ORNs was observed in *Drosophila* ORNs (***Getahun et al., 2013***) and with heterologously expressed OR-Orco proteins (***Mukunda et al., 2016***). This OR sensitization process requires Orco activity and was proposed to depend on cAMP production that would activate two feedback loops involving protein kinase and Ca^{2+}-calmodulin (***Wicher, 2018***).

Mechanism of the spike frequency adaptation

In *Drosophila melanogaster*, adaptation properties could be captured with a bi-lobed linear filter with a temporal width of approximately 200 ms (***Nagel and Wilson, 2011***; ***Martelli et al., 2013***; see ***Brandão et al., 2021*** for a recent review). Studies of ORN adaptation in moths suggest that their adaptation is slower (***Jacob et al., 2017***; ***Levakova et al., 2019***). However, the moth studies related the firing activity to the binary state of the electrovalves controlling the odor delivery, it is therefore difficult to assess to what extent the observed signal processing timescales are a property of the odor delivery device or a property of the neuron.

We circumvented this issue by simultaneously measuring the local field potential (LFP) in the sensilla, where the ORN's outer dendrite resides. The LFP is tightly correlated with the depolarizing current entering the ORN. We built a model of transformation of the depolarizing current to the spiking activity and performed an optimization procedure which allowed us to narrow down the adaptation processes to only two time-scales, which are not directly inferable from the linear filters and importantly, provide novel insights into the possible mechanisms leading to the adaptation.

We showed that the shape of the ORN's firing response can be very well captured with only two adaptation time scales: 40 ms and 800 ms. This is the minimal model capable of explaining the transiency of the firing response and the observed temporal resolution limits of the ORN.

The slow adaptation time constant 800 ms approximately corresponds to Ca^{2+} extrusion time scales (0.4 s to 1 s in *Drosophila* ORNs; ***Si et al., 2019***). This indicates that the adaptation of the spike generating mechanism could be Ca^{2+} dependent. Moth ORNs express Ca^{2+}-gated potassium channels (***Lucas and Shimahara, 2002*** in *Mamestra brassicae*; ***Zufall et al., 1991*** in *Manduca sexta*; ***Pézier et al., 2007*** in *S. littoralis*). Their expression in the soma would result in hyperpolarizing currents upon their activation.

Inactivation of voltage gated sodium channels (Na_V) could also be responsible for the phasicity of the spiking response (***Lundstrom et al., 2008***; ***Platkiewicz and Brette, 2010***, ***2011***; ***Nagel and Wilson, 2011***). However, the timescales typical for inactivation (and reactivation) of Na_V channels (4.8 ms measured in cultured honeybee ORNs (***Kadala et al., 2011***)) were not necessary to reproduce the firing rate profiles. Some Na_V channels also exhibit adaptation at slower time scales (***Fleidervish et al., 1996***; ***Kim and Rieke, 2003***; ***Badel et al., 2008***; ***Wang et al., 2013***; ***Sarno et al., 2022***). Patch clamp experiments on insect ORNs designed to measure slow adaptation of Na_V channels in insect ORNs would help to understand the physiological mechanisms behind their adaptation.

Modelling the ORN response

We proposed a minimal model that links the stimulus to the firing rate which captures well the firing profile of responses to isolated square pulses. This model can be easily used to model the input to the higher brain centers, which is otherwise often modelled as a piece-wise exponential function (***Belmabrouk et al., 2011***; ***Tuckman et al., 2021a***,b). It can be extended to model the responses to more complex stimuli; however, the model captures all the features essential for our work. The following extensions could be considered:

1. Adaptation of the odor receptors
2. Persistent receptor activity
3. Nonlinearity of the slow adaptation process

Various receptor adaptation models were proposed for *Drosophila* ORNs (***Nagel and Wilson, 2011***; ***Cao et al., 2016***; ***Gorur-Shandilya et al., 2017***) and we believe that these models could be also successfully applied to the moth ORNs. However, in the case of moth, the long lasting pheromone transduction pathway (due to pheromone adherence to the sensilla and / or sustained increased probability of spontaneous receptor opening) needs to be included as well to balance the adaptation and maintain receptor activity after the stimulus offset and avoid transient LFP overshoot, as observed in some *Drosophila* ORNs (***Nagel and Wilson, 2011***). It is also possible that the physics of

fluid (air) movement across morphologically distinct antennal types (globular in *Drosophila*, feather-like in *A. ipsilon*), and the wingbeat frequency of the insect (200 Hz in *Drosophila*, 5 Hz to 20 Hz in moths) that re-sculpt the odor plume could have both contributed to the evolution of the differentiated transduction process.

Our linear-nonlinear model predicts well the time course of the firing rate during stimulation and its offset after stimulus termination. However, the predicted duration of the inhibitory period is longer than what we generally observe. We believe that this can be explained by a voltage dependency of the slow adaptation process. Such non-linearity seems plausible, since either the Na_V channels can recover faster at low membrane potential values, or the voltage dependency of the Ca^{2+}-gated K^+ channels causes them to close rapidly at low membrane potential values (***Lucas and Shimahara, 2002***).

Implications for behavior and navigation efficiency

Behavioral experiments showed that male moths reach the pheromone source most reliably and with the least amount of counter-turning if the source is pulsating (***Kennedy et al., 1980***; ***Willis and Baker, 1984***; ***Mafra-Neto and Cardé, 1994***). Particularly, in (***Mafra-Neto and Cardé, 1994***), the pulse duration was 130 ms and the air-gap duration between pulses was 83 ms (experiments done with the almond moth *Cadra cautella*). These observations correlate well with our results showing that the ORNs exhibit prolonged firing response to short (<200 ms) stimuli. Moreover, prolonged response to very short stimuli (e.g., 3 ms) can ensure that the brief encounter is registered by the brain and can be acted upon.

On the other hand, the slow (800 ms) adaptation allows the moth to respond rapidly to a loss of pheromone signal after a prolonged exposure, but possibly also to adapt to the background intensity within a pheromone plume. If the prolonged firing response to short stimuli causes prolonged upwind flight after stimulus offset, we expect faster switching from upwind flight to zig-zag casting after the stimulus offset with longer stimuli. Such behavioral experiments could show a clear connection between the temporal structure of the ORN and PN response and behavior.

Materials and methods

Insects

A. ipsilon and *S. littoralis* adult males were fed on an artificial diet. Pupae were sexed and males and females were kept separately in an inversed light–dark cycle (16 h:8 h light:dark photoperiod) at 22 °C. Experiments were carried out on 5-day-old males.

Chemicals

The main components of the pheromones of *A. ipsilon* (Z7-12:Ac, CAS 14959-86-5) and *S. littoralis* (Z9,E11-14:Ac, CAS 50767-79-8) were bought from Pherobank (purity > 99%). Linalool (CAS 78-70-6, purity > 97%,) α-pinene (CAS 80-56-8, purity >98%) and acetone (CAS 67-64-1) were bought from Sigma-Aldrich. They were diluted at 10% in mineral oil (CAS 8012-95-1).

Odor delivery

Our odor delivery device is based on 2 serially connected electrovalves. The first electrovalve (any of EV1 - EV8, further referred to as upstream valve) odorizes the passing airflow. The second electrovalve (EV9, downstream valve) controls the timing of the stimulus (***Figure 1–Figure Supplement 1***).

A charcoal-filtered and humidified air stream (2.5 bar) is divided into 8 flows (200 mL/min each) with an airflow divider (LFMX0510528B, The Lee Company, Westbrook, CT, USA). Each of the 8 flows is connected to a 3-way electrovalve (EV1 to EV8; LHDA1223111H, The Lee Company). Normally opened (NO, non-odorized) and normally closed (NC, odorized) exits of the eight valves are connected to a low dead-volume manifold (MPP-8, Warner Instruments, Holliston, MA, USA) or to

odor sources, respectively. The non-odorized airflow permanently bathes the insect preparation. All outlets of odor sources are connected to a second MPP-8 manifold that is connected to an electrovalve (EV9; LHDA1233215H, The Lee Company). The NO exit of EV9 is introduced within a vacuum system. A small glass tube (10 mm total length, 1.16 mm internal diameter) bent at 90° facilitated focusing the stimuli on the insect antenna. EV9 and the small bent tube are thus the sole surface on which odor puffs controlled by EV9 can adsorb and thus alter the stimulus dynamics. The outlet of the small tube is positioned under the dissecting microscope at 1 mm from the recorded sensilla. An aluminium shield connected to the ground around EV9 minimizes artifacts during opening and closing of the valve. The downstream part of the stimulator (from manifold to EV9 and the attached small bent tube) was decontaminated after each experiment for 60 min at 80 °C with an airflow injected from the small bent tube and EV9 activated. All tubing but the exit of the permanent airflow was made of Teflon (internal diameter 1.32 mm). The shape of stimuli delivered to the antenna was measured with a mini PID (Aurora Scientific Inc, Aurora, Canada).

Equilibration and stability of the odor source

After opening the upstream electrovalve two processes are at play when an airflow passes through the odor source, with opposite effects on the concentration of odor reaching the downstream electrovalve, EV9.

1. Dilution of the head-space, which reduces the concentration of odor delivered to EV9 with an effect that increases with time until an asymptote is reached corresponding to an equilibrium of odor molecules passing from the liquid phase to the gas phase and those carried out of the vial by the airflow.
2. Reversible binding of odor molecules to the surfaces of the odor delivery device, which reduces the concentration of odor delivered to EV9 with an effect that gradually decreases over time until it becomes null when the adsorption/desorption equilibrium is reached.

We verified with linalool (diluted at 10%) and the PID how long the upstream valve must be open before the odor concentration delivered to the downstream valve is constant (further referred to as equilibration time). With no or short equilibration times (≤2 s), PID responses were not square but had a decreasing amplitude indicating that the dilution of head-space was dominant. When the equilibrium time was at least 10 s, the PID response to a 0.5 s stimulus was square. Increasing the equilibration time to more than 10 s had very little effect on the amplitude of the PID response (***Figure 1–Figure Supplement 2***A-B). When using α-pinene and acetone, more volatile molecules than linalool, we kept the same 10 s equilibration time.

Since the PID cannot monitor pheromone stimuli, the equilibration time with pheromone was adjusted by measuring the amplitude of SSR responses to a 0.5 s stimulus with 100 pg of Z7-12:Ac. Equilibration times of 1 s, 3 s, 10 s, 30 s, 78 s were tested both in ascending and descending order. Stimuli were applied every 2 min. Equilibrations were stopped at each stimulus offset. The amplitude of responses increased for equilibration times of 1 s to 30 s and then remained stable, indicating that the odor binding to surfaces was the dominant effect (***Figure 1–Figure Supplement 2***C). We thus kept an equilibration time of 30 s for further experiments.

We then measured the stability of the pheromone source first by applying 9 stimuli with 100 pg of Z7-12:Ac. Each stimulus was preceded by an equilibration time of 30 s. The inter stimulus interval was 2 min. The amplitude of responses remained constant over the 9 stimuli (***Figure 1–Figure Supplement 2***D).

Single sensillum recordings

For single sensillum recordings, male moths were briefly anesthetized with CO_2 and restrained in a Styrofoam holder. One antenna was immobilized with adhesive tape.

Single sensillum recordings were carried out either with tungsten electrodes or with glass electrodes, the later allowing to record the local field potential (LFP) in addition to the firing response

Table 1. Number of sensilla recorded for each pulse duration. Number of neurons that responded by firing at least 5 spikes in the first 100 ms after stimulus onset is in the brackets.

pulse duration:	3 ms	5 ms	10 ms	20 ms	50 ms	100 ms
	22 (7)	22 (13)	23 (21)	22 (20)	21 (20)	23 (22)

pulse duration:	200 ms	500 ms	1 s	2 s	5 s
	23 (22)	23 (23)	23 (22)	23 (22)	23 (22)

Table 2. Number of sensilla recorded for each duration-dose pair. Number of neurons that responded by firing at least 5 spikes in the first 100 ms after stimulus onset is in the brackets.

	20 ms	200 ms	2 s
10 pg	57 (28)	57 (32)	57 (32)
100 pg	55 (33)	56 (44)	54 (38)
1 ng	53 (40)	52 (39)	52 (41)

of ORNs. In both cases, one electrode was inserted into the antenna to serve as a reference. We targeted the ORNs tuned to the pheromone constituent Z7-12:Ac. The recording electrode was inserted at the base of one of the long trichoid sensilla located along antennal branches, the vast majority of which house an ORN tuned to the major pheromone component Z7-12:Ac. The reference electrode was inserted in an antennal segment next to the one bearing the recorded sensillum. Recordings were done using a CyberAmp 320 controlled by pCLAMP10 (Molecular Devices, San Jose, CA, USA). The signal was amplified ($\times 100$), band-pass filtered (10 Hz to 3000 Hz) with tungsten electrodes or low-pass filtered (3000 Hz) with glass electrodes and sampled at 10 kHz with a Digidata 1440A acquisition board (Molecular Devices). Spikes were sorted using Spike 2 software (CED, Oxford, Great Britain).

Experimental protocols

To record the firing responses to pulses of different durations (***Figure 2***), we performed recordings with tungsten electrode from 23 sensilla and presented them with stimuli of durations 3 ms, 5 ms, 10 ms, 20 ms, 50 ms, 100 ms, 200 ms, 500 ms, 1 s, 2 s and 5 s (pheromone dose 100 pg) in a randomized order. There was a 2 min gap between stimuli. The number of recorded responses varies for each duration and is provided in ***Table 1***.

To test the responses to different pheromone doses (***Figure 3***), we performed recordings with tungsten electrodes from 57 sensilla, presenting them with pulses of durations 20 ms, 200 ms and 2 s in a randomized order, but with an increasing pheromone dose. The number of responses recorded for each duration-dose pair is provided in ***Table 2***.

We recorded the LFP simultaneously with the spiking activity for the pulse durations 20 ms, 200 ms and 2 s, presented in randomized order with 3 min inter-stimulus intervals (dose 1 ng). In some recordings with the glass electrode we observed a significant change in the shape of the firing response; particularly, the neurons started responding more tonically with time and did not exhibit the inhibitory period after 2 s pulse anymore. We assume that this is due to the glass electrode being more invasive than the sharper tungsten electrode, modifying the composition of the sensillar lymph and/or damaging the ORN. Therefore, in order to exclude neurons whose functioning was altered, we presented one more 2 s pulse after the the initial three pulses and included the recording in the analysis only if the second response to the 2 s pulse exhibited the inhibitory phase (here defined as zero spikes during the interval 50 ms to 500 ms). In total, we used 26 out of 37 recordings, therefore 26 responses for each duration. To filter out the LFP without action

potentials we used a 15 Hz 2-pole Butterworth low-pass filter.

For the experiments using TTX, the drug was dissolved (50 µM) in saline (in mM: NaCl 154, KCl 3, glucose 24) and injected into the body of the antenna using a syringe-driven glass micropipette. Controls were saline injections. Recordings started 5 min after injection. The firing activity was completely abolished after all TTX injections and remained intact after saline injections.

Data analysis

Firing frequency

We estimated the firing rates by the kernel density estimation method. Each spike was substituted with a normal distribution probability distribution function with mean at the spike time and standard deviation $\sigma = \frac{\mathrm{bw}}{2}$, where bw is the kernel width.

In ***Figure 2*** we used a time dependent kernel width in order to depict the responses to short stimuli with sufficient detail, but avoid high noise when the firing rate drops during longer stimulation. The time dependence was given by:

$$\mathrm{bw}(t) = \begin{cases} \mathrm{bw}_{\min} & t < 0, \\ \mathrm{bw}_{\max} - \mathrm{bw}_{\min} \exp\left(-t/\tau_{\mathrm{KDE}}\right) + \mathrm{bw}_{\min} & t > 0, \end{cases} \tag{6}$$

where $\mathrm{bw}_{\min} = 10\,\mathrm{ms}$, $\mathrm{bw}_{\max} = 100\,\mathrm{ms}$, $\tau_{\mathrm{KDE}} = 500\,\mathrm{ms}$ and we assume that the stimulus onset is at 0.

Response end of individual ORNs

The first inter-spike interval (ISI) that finishes after the stimulus offset and exceeds 100 ms is considered as the terminating ISI and the initiating AP as the time of the response end. We calculated the response end only if the neuron fired at least 5 action potentials during the first 100 ms after the stimulus onset (numbers of responding neurons provided in brackets in ***Table 1*** and ***Table 2***). We then calculated the time of the response end for a group of neurons as the median of individual response ends (red vertical lines in ***Figure 2*** and ***Figure 3***). Note that if the ISI after the last spike during stimulation is longer than 100 ms, the calculated response end for the ORN is before the stimulus end.

Linear-nonlinear model for firing rate prediction

We used linear regression to predict the firing rate. As independent variables, we used values of the past LFP convolved with a gamma distribution-shaped function with different time constants and shape parameters (***Gorur-Shandilya et al., 2017***; ***Jayaram et al., 2022***):

$$x(t;\tau,\alpha) = \int_0^{+\infty} V(t-s)\frac{1}{\Gamma(\alpha)\tau^{\alpha}} t^{\alpha-1} e^{-\frac{t}{\tau}}\,\mathrm{d}s, \tag{7}$$

where V is the LFP. The model is then specified by the time constants τ_1, ..., τ_n and the corresponding shape parameters α_1, ..., α_n. The estimated firing rate before the non-linearity is specified by the coefficients c_1, ..., c_n:

$$f(t) = \sum_{k=1}^{n} c_k x(t;\tau_k). \tag{8}$$

We estimated the coefficients with the least square method to provide the estimate of firing rate (estimated from the spike train with kernel width 30 ms) during the 2 s stimulus and 1 s of the preceding spontaneous activity.

In order to choose the time constants and shapes specifying the model, we initially used a model with 20 time constant, ranging from 1 ms to 3 s, equidistantly spaced on the logarithmic scale. Moreover, we used 17 different gamma distribution shapes α ranging from 1 to 5, equidistantly spaced. The model then contained 20×17 independent variables. We fit the model to the average LFP and average firing rate response during 2 s stimulus with lasso regression (optimal L1 penalty parameter was selected with cross-validation using the LassoCV regressor in Scikit-learn

(***Pedregosa et al., 2011***)). The non-zero coefficients then concentrated around several (α, τ) pairs, but mostly at the $\alpha = 1$ edge, from which we selected the three time constants with $\alpha = 1$, i.e., exponential kernels (1 ms, 40 ms, 800 ms, ***Figure 5–Figure Supplement 2***A). For simplicity, we substituted the kernel with $\tau = 1\,\mathrm{ms}$ with a δ-function.

Although the filter obtained from the full lasso regression looks different from the filters obtained with only three exponential kernels (***Figure 5–Figure Supplement 2***B-C), the predicted firing rates are nearly identical (***Figure 5–Figure Supplement 2***D-F).

Modelling odor transduction

We modelled the transduction described by ***Equation 4*** by a set of differential equations:

$$\frac{\mathrm{d}}{\mathrm{d}t}\mathrm{R} = s_b \cdot \mathrm{OR} - [\mathrm{O}]k_b s_b \cdot \mathrm{R}, \tag{9}$$

$$\frac{\mathrm{d}}{\mathrm{d}t}\mathrm{OR} = [\mathrm{O}]k_b s_b \cdot \mathrm{R} + s_a \cdot \mathrm{OR}^* - k_a s_a \cdot \mathrm{OR} - s_b \cdot \mathrm{OR}, \tag{10}$$

$$\frac{\mathrm{d}}{\mathrm{d}t}\mathrm{OR}^* = -s_a \cdot \mathrm{OR}^* + k_a s_a \cdot \mathrm{OR}, \tag{11}$$

$$\frac{\mathrm{d}}{\mathrm{d}t}\mathrm{LFP} = -\frac{1}{\tau_{\mathrm{LFP}}}(\mathrm{LFP} - \beta \cdot \mathrm{OR}^*). \tag{12}$$

R, OR and OR* indicate the ratios of unbound, bound and activated bound receptors, $\tau_{\mathrm{LFP}} = 10\,\mathrm{ms}$. The initial conditions are $\mathrm{R} = 1$ and $\mathrm{OR} = \mathrm{OR}^* = \mathrm{LFP} = 0$. We modelled the odor concentration as a square odor pulse: $[\mathrm{O}] = 10^{-11}\,\mathrm{M}$ during stimulation and 0 otherwise. Because we did not attempt to model the adaptation and the sustained activity (more important with long stimuli), we fitted the parameters s_b, k_b, s_a, k_a and β to the first 400 ms after stimulus onset of the average LFP from 20 ms and 200 ms stimulations. We fitted the parameters by minimizing the square error of the prediction with the L-BFGS-B algorithm implemented in SciPy (***Virtanen et al., 2020***). The fitted model parameters are $k_a = 6.57 \cdot 10^{11}\,\mathrm{s}^{-1}\mathrm{M}^{-1}$, $s_a = 7.36\,\mathrm{s}^{-1}$, $k_b = 37.3$, $s_b = 131\,\mathrm{s}^{-1}$, $\beta = -5.67\,\mathrm{mV}$.

Antennal lobe model

We used a model of a single glomerulus from the AL model proposed by ***Tuckman et al.*** (***2021a***). In the following, we explicitely state when we deviate from the established model.

The glomerulus contained 10 PNs and 6 LN. The membrane potential dynamics of i-th PN and j-th LN were governed by the following dynamics:

$$\frac{\mathrm{d}}{\mathrm{d}t}V^i_{\mathrm{PN}} = -\frac{1}{\tau_V}(V^i_{\mathrm{PN}} - E_L) - g^i_{\mathrm{SK}}(t)(V^i_{\mathrm{PN}} - E_{\mathrm{SK}}) - g^i_{\mathrm{stim}}(t)(V^i_{\mathrm{PN}} - E_{\mathrm{stim}}) - \\ - g^i_{\mathrm{exc}}(t)(V^i_{\mathrm{PN}} - E_{\mathrm{exc}}) - g^i_{\mathrm{inh}}(t)(V^i_{\mathrm{PN}} - E_{\mathrm{inh}}) - g^i_{\mathrm{slow}}(t)(V^i_{\mathrm{PN}} - E_{\mathrm{inh}}), \tag{13}$$

$$\frac{\mathrm{d}}{\mathrm{d}t}V^j_{\mathrm{LN}} = -\frac{1}{\tau_V}(V^j_{\mathrm{LN}} - E_L) - g^j_{\mathrm{stim}}(t)(V^j_{\mathrm{LN}} - E_{\mathrm{stim}}) - \\ - g^j_{\mathrm{exc}}(t)(V^j_{\mathrm{LN}} - E_{\mathrm{exc}}) - g^j_{\mathrm{inh}}(t)(V^j_{\mathrm{LN}} - E_{\mathrm{inh}}) - g^j_{\mathrm{slow}}(t)(V^i_{\mathrm{LN}} - E_{\mathrm{inh}}), \tag{14}$$

where τ_V is the membrane time constant, g_{SK} is the conductance of SK channels, g_{stim} is the excitatory conductance associated with the ORN input, g_{exc} is the excitatory synaptic conductance from PNs, g_{inh} is the fast inhibitory $\mathrm{GABA_A}$ conductance, g_{slow} is the slow $\mathrm{GABA_B}$ conductance. E_{SK}, E_{stim}, E_{exc}, E_{inh} are the reversal potentials associated with these conductances, E_L is the leak reversal potential. The reversal potentials are expressed in nondimensional units: $E_L = 0$, $E_{\mathrm{exc}} = E_{\mathrm{stim}} = \frac{14}{3}$, $E_{\mathrm{SK}} = E_{\mathrm{inh}} = -\frac{2}{3}$. The neuron fires a spike then the membrane potential V reaches the threshold $V_{\mathrm{thr}} = 1$ and is then reset to E_L and held at E_L for τ_{ref}. The synaptic conductances g_X, $X \in \{\mathrm{exc}, \mathrm{inh}, \mathrm{slow}, \mathrm{stim}\}$ follow the equation

$$\tau_X \frac{\mathrm{d}}{\mathrm{d}t}g^i_X = -g^i_X + S_X \sum_{t_{\mathrm{spike}} \in \{t^i_X\}} \delta(t - t_{\mathrm{spike}}), \tag{15}$$

Table 3. Synaptic connection amplitudes.

	S_{exc}	S_{inh}	S_{slow}	S_{stim}
PN	0.01	0.0169	0.0338	0.004
LN	0.006	0.015	0.04	0.0031

Table 4. Neuron connection probabilities.

PN→PN	PN→LN	LN→PN	LN→LN
0.75	0.75	0.38	0.25

where $\{t_X^i\}$ represents the corresponding presynaptic spikes to the i-th, τ_X is the synaptic time constant for the given synapse type and the conductance increases by $\tau_X S_X$ with each presynaptic spike arrival. S_X differ for PNs and LNs and are specified in ***Table 3***.

The SK conductance g_{SK} was modelled only for the PNs and did not rise instantaneously, instead followed the equations:

$$\tau_{\text{rise}} \frac{\mathrm{d}}{\mathrm{d}t} g_{\text{SK}}^i = -(g_{\text{SK}}^i - z), \tag{16}$$

$$\tau_{\text{SK}} \frac{\mathrm{d}}{\mathrm{d}t} z = -z + S_{\text{SK}} \sum_{t_{\text{spike}} \in \{t^i\}} \delta(t - t_{\text{spike}}), \tag{17}$$

where τ_{rise} characterizes the rise time, τ_{SK} is the decay time constant of the SK conductance and $\{t^i\}$ is the set of spikes fired by the i-th PN. Note that here, for simulation purposes, we deviate from the original model (***Tuckman et al., 2021a***) by modelling g_{SK}^i with a set of two equations instead of modelling the time course of g_{SK}^i following a single spike as a piece-wise function. S_{SK}^i was drawn from a normal distribution with mean $\mu = 0.5$ and $\sigma = 0.2$ (negative values were set to 0).

The connection between the neurons within the glomerulus were random with probabilities specified in ***Table 4***.

To model the ORN input, we generated the spike trains of 10^4 ORNs from an inhomogeneous Poisson process, each ORN connects to any AL neuron with a 1% probability. The time course of each ORN was given by the average ORN firing rate (***Figure 2***, note that the input therefore differs from (***Tuckman et al., 2021a***)). We also added a constant ORN input of 30 Hz as a means to increase the spontaneous activity, as observed in experiments (***Jarriault et al., 2010***).

We simulated the network using the Brian 2 Python package (***Stimberg et al., 2019***).

Multicompartmental ORN model

The model is a simplified version of the moth pheromone transduction model by ***Gu et al.*** (***2009***). From this model we kept the morphology and the passive conductances (***Figure 4–Figure Supplement 1***). The following set of equations describes the evolution of the potentials in the individual compartments:

$$\frac{dV_{id}}{dt} = \frac{G_e}{C_{md}(G_e+G_i)}(I_R + I_{ld} - I_e) + \frac{G_e}{C_{ma}(G_e+G_i)}(I_a - I_e) + \frac{G_i}{C_{ms}(G_e+G_i)}(I_i - I_{ls} - I_{ad}), \quad (18)$$

$$\frac{dV_{ed}}{dt} = \frac{G_i}{C_{md}(G_e+G_i)}(I_e - I_R - I_{ld}) + \frac{G_e}{C_{ma}(G_e+G_i)}(I_a - I_e) + \frac{G_i}{C_{ms}(G_e+G_i)}(I_i - I_{ls} - I_{ad}), \quad (19)$$

$$\frac{dV_{is}}{dt} = \frac{I_i - I_{ls} - I_{ad}}{C_{ms}}, \quad (20)$$

$$\frac{dV_{ea}}{dt} = \frac{I_a - I_e}{C_{ma}}. \quad (21)$$

Where the currents are described by:

$$I_{ls} = G_{ls}(V_{is} - E_{ls}), \quad (22)$$

$$I_{ld} = G_{ld}(V_{ed} - V_{id} + E_{ld}), \quad (23)$$

$$I_i = G_i(V_{id} - V_{is}), \quad (24)$$

$$I_a = -G_a(V_{ea} + E_a), \quad (25)$$

$$I_e = G_e(V_{ea} - V_{ed}). \quad (26)$$

I_R is the receptor current, which we either calculated by fixing the LFP (V_{ed}) and calculating what receptor current I_R is necessary to produce given LFP time course, or we fixed the I_R time course. To estimate I_R from given LFP, we substituted ***Equation 19*** by the numerical derivative of the LFP and expressed I_R using the numerical derivative to use in ***Equation 18***.

I_{ad} is the adaptation current. We considered $I_{ad} \neq 0$ only to illustrate the effect of adaptation currents in the soma on the LFP. In such case, we fixed the input I_R to the model and fixed the time course of the somatic membrane potential V_{is} to correspond to the shape of the firing rate (again, by calculating its numerical derivative and eliminating ***Equation 20***). Then we calculated the necessary I_{ad} to balance the depolarizing effect of I_R.

We simulated the multicompartmental model with the explicit Runge-Kutta method of order 5(4) with upper limit on integration step 0.1 ms implemented in SciPy (***Virtanen et al., 2020***). We used the initial conditions $V_{ed} = V_{ea} = -35\,\mathrm{mV}$, $V_{id} = V_{is} = -62\,\mathrm{mV}$. This condition corresponds to $I_e = I_{ld} = I_i = I_{ls} = I_a = 0$, given that $I_R = I_{ad} = 0$.

Acknowledgments

We are grateful to Claude Collet for a helpful discussion on sodium channels in the insect olfactory system and to Vincent Jacob for critical reading of the manuscript. This work was supported by the Charles University, project GA UK No. 1042120 and the Czech Science Foundation project 20-10251S. TB benefited from a fellowship from the Plant Health and Environment Division of INRAE.

References

Anderson MJ, Sullivan JG, Horiuchi TK, Fuller SB, Daniel TL. A bio-hybrid odor-guided autonomous palm-sized air vehicle. Bioinspir Biomim. 2020 3; 16(2):026002. doi: 10.1088/1748-3190/abbd81.

Ando N, Emoto S, Kanzaki R. Odour-tracking capability of a silkmoth driving a mobile robot with turning bias and time delay. Bioinspir Biomim. 2013 2; 8(1):016008. doi: 10.1088/1748-3182/8/1/016008.

Angioy AM, Desogus A, Barbarossa IT, Anderson P, Hansson BS. Extreme Sensitivity in an Olfactory System. Chem Senses. 2003 5; 28(4):279–284. doi: 10.1093/chemse/28.4.279.

Badel L, Lefort S, Brette R, Petersen CCH, Gerstner W, Richardson MJE. Dynamic I-V Curves Are Reliable Predictors of Naturalistic Pyramidal-Neuron Voltage Traces. J Neurophysiol. 2008 2; 99(2). doi: 10.1152/jn.01107.2007.

Belmabrouk H, Nowotny T, Rospars JP, Martinez D. Interaction of cellular and network mechanisms for efficient pheromone coding in moths. Proc Natl Acad Sci USA. 2011 12; 108(49). doi: 10.1073/pnas.1112367108.

Brandão SC, Silies M, Martelli C. Adaptive temporal processing of odor stimuli. Cell Tissue Res. 2021 1; 383(1):125–141. doi: 10.1007/s00441-020-03400-9.

van Breugel F, Dickinson MH. Plume-Tracking Behavior of Flying Drosophila Emerges from a Set of Distinct Sensory-Motor Reflexes. Curr Biol. 2014 2; 24(3):274–286. doi: 10.1016/j.cub.2013.12.023.

Budick SA, Reiser MB, Dickinson MH. The role of visual and mechanosensory cues in structuring forward flight in *Drosophila melanogaster*. J Exp Biol. 2007 12; 210(23):4092–4103. doi: 10.1242/jeb.006502.

Cao LH, Jing BY, Yang D, Zeng X, Shen Y, Tu Y, Luo DG. Distinct signaling of *Drosophila* chemoreceptors in olfactory sensory neurons. Proc Natl Acad Sci USA. 2016 2; 113(7). doi: 10.1073/pnas.1518329113.

Cardé RT, Charlton RE. Olfactory sexual communication in Lepidoptera: strategy, sensitivity and selectivity. In: Lewis T, editor. *Insect communication* London: Academic press; 1984.p. 241–265.

Cardé RT. Navigation Along Windborne Plumes of Pheromone and Resource-Linked Odors. Annu Rev Entomol. 2021 1; 66(1):317–336. doi: 10.1146/annurev-ento-011019-024932.

Celani A, Villermaux E, Vergassola M. Odor Landscapes in Turbulent Environments. Phys Rev X. 2014 10; 4(4):041015. doi: 10.1103/PhysRevX.4.041015.

Dieudonné A, Daniel TL, Sane SP. Encoding properties of the mechanosensory neurons in the Johnston's organ of the hawk moth, *Manduca sexta*. J Exp Biol. 2014 1; doi: 10.1242/jeb.101568.

Elkinton JS, Schal C, Onot T, Cardé RT. Pheromone puff trajectory and upwind flight of male gypsy moths in a forest. Physiol Entomol. 1987 12; 12(4):399–406. doi: 10.1111/j.1365-3032.1987.tb00766.x.

Fleidervish IA, Friedman A, Gutnick MJ. Slow inactivation of Na^+ current and slow cumulative spike adaptation in mouse and guinea-pig neocortical neurones in slices. J Physiol (Lond). 1996 5; 493(1). doi: 10.1113/jphysiol.1996.sp021366.

Getahun MN, Olsson SB, Lavista-Llanos S, Hansson BS, Wicher D. Insect Odorant Response Sensitivity Is Tuned by Metabotropically Autoregulated Olfactory Receptors. PLoS ONE. 2013 3; 8(3):e58889. doi: 10.1371/journal.pone.0058889.

Gorur-Shandilya S, Demir M, Long J, Clark DA, Emonet T. Olfactory receptor neurons use gain control and complementary kinetics to encode intermittent odorant stimuli. eLife. 2017; 6:e27670. doi: https://doi.org/10.7554/eLife.27670.001.

Gorur-Shandilya S, Martelli C, Demir M, Emonet T. Controlling and measuring dynamic odorant stimuli in the laboratory. J Exp Biol. 2019 12; 222(23):jeb207787. doi: 10.1242/jeb.207787.

Grémiaux A, Nowotny T, Martinez D, Lucas P, Rospars JP. Modelling the signal delivered by a population of first-order neurons in a moth olfactory system. Brain Res. 2012 1; 1434. doi: 10.1016/j.brainres.2011.09.035.

Gu Y, Lucas P, Rospars JP. Computational Model of the Insect Pheromone Transduction Cascade. PLoS Comput Biol. 2009 3; 5(3):e1000321. doi: 10.1371/journal.pcbi.1000321.

Jacob V, Monsempès C, Rospars JP, Masson JB, Lucas P. Olfactory coding in the turbulent realm. PLoS Comput Biol. 2017 12; 13(12):e1005870. doi: 10.1371/journal.pcbi.1005870.

Jarriault D, Gadenne C, Lucas P, Rospars JP, Anton S. Transformation of the Sex Pheromone Signal in the Noctuid Moth *Agrotis ipsilon*: From Peripheral Input to Antennal Lobe Output. Chem Senses. 2010 10; 35(8):705–715. doi: 10.1093/chemse/bjq069.

Jayaram V, Kadakia N, Emonet T. Sensing complementary temporal features of odor signals enhances navigation of diverse turbulent plumes. eLife. 2022 1; 11. doi: 10.7554/eLife.72415.

Jones CD. On the structure of instantaneous plumes in the atmosphere. J Hazard Mat. 1983 1; 7(2):87–112. doi: 10.1016/0304-3894(83)80001-6.

Justus KA, Murlis J, Jones C, Cardé RT. Measurement of odor-plume structure in a wind tunnel using a photoionization detector and a tracer gas. Environ Fluid Mech. 2002; 2(1/2). doi: 10.1023/A:1016227601019.

Kadala A, Charreton M, Jakob I, Le Conte Y, Collet C. A use-dependent sodium current modification induced by type I pyrethroid insecticides in honeybee antennal olfactory receptor neurons. Neurotoxicology. 2011 6; 32(3):320–330. doi: 10.1016/j.neuro.2011.02.007.

Kaissling KE, Meng LZ, Bestmann HJ. Responses of bombykol receptor cells to (Z,E)-4,6-hexadecadiene and linalool. J Comp Physiol A. 1989 3; 165(2):147–154. doi: 10.1007/BF00619189.

Kaissling KE. The Sensitivity of the Insect Nose: The Example of *Bombyx Mori*. In: *Biologically inspired signal processing* Springer Verlag; 2009.p. 45–52. doi: 10.1007/978-3-642-00176-5{_}3.

Kaissling KE, Priesner E. Die Riechschwelle des Seidenspinners. Sci Nat. 1970 1; 57(1):23–28. doi: 10.1007/BF00593550.

Kay LM, Stopfer M. Information processing in the olfactory systems of insects and vertebrates. Semin Cell Dev Biol. 2006 8; 17(4):433–442. doi: 10.1016/j.semcdb.2006.04.012.

Kennedy JS. Zigzagging and casting as a programmed response to wind-borne odour: a review. Physiol Entomol. 1983 6; 8(2):109–120. doi: 10.1111/j.1365-3032.1983.tb00340.x.

Kennedy JS, Ludlow AR, Sanders CJ. Guidance system used in moth sex attraction. Nature. 1980 12; 288(5790):475–477. doi: 10.1038/288475a0.

Kim AJ, Lazar AA, Slutskiy YB. System identification of *Drosophila* olfactory sensory neurons. J Comput Neurosci. 2011 2; 30(1). doi: 10.1007/s10827-010-0265-0.

Kim AJ, Lazar AA, Slutskiy YB. Projection neurons in *Drosophila* antennal lobes signal the acceleration of odor concentrations. eLife. 2015 5; 4. doi: 10.7554/eLife.06651.

Kim KJ, Rieke F. Slow Na^+ Inactivation and Variance Adaptation in Salamander Retinal Ganglion Cells. J Neurosci. 2003 2; 23(4):1506–1516. doi: 10.1523/JNEUROSCI.23-04-01506.2003.

Kostal L, Lansky P, Rospars JP. Efficient olfactory coding in the pheromone receptor neuron of a moth. PLoS Comput Biol. 2008; 4:e1000053.

Levakova M, Kostal L, Monsempès C, Jacob V, Lucas P. Moth olfactory receptor neurons adjust their encoding efficiency to temporal statistics of pheromone fluctuations. PLoS Comput Biol. 2018 11; 14(11):e1006586. doi: 10.1371/journal.pcbi.1006586.

Levakova M, Kostal L, Monsempès C, Lucas P, Kobayashi R. Adaptive integrate-and-fire model reproduces the dynamics of olfactory receptor neuron responses in a moth. J R Soc Interface. 2019 8; 16(157):20190246. doi: 10.1098/rsif.2019.0246.

Lucas P, Shimahara T. Voltage- and Calcium-activated Currents in Cultured Olfactory Receptor Neurons of Male *Mamestra brassicae* (Lepidoptera). Chem Senses. 2002 9; 27(7):599–610. doi: 10.1093/chemse/27.7.599.

Lundstrom BN, Hong S, Higgs MH, Fairhall AL. Two Computational Regimes of a Single-Compartment Neuron Separated by a Planar Boundary in Conductance Space. Neural Comput. 2008 5; 20(5):1239–1260. doi: 10.1162/neco.2007.05-07-536.

Mafra-Neto A, Cardé RT. Fine-scale structure of pheromone plumes modulates upwind orientation of flying moths. Nature. 1994 5; 369(6476):142–144. doi: 10.1038/369142a0.

Martelli C, Carlson JR, Emonet T. Intensity Invariant Dynamics and Odor-Specific Latencies in Olfactory Receptor Neuron Response. J Neurosci. 2013 4; 33(15). doi: 10.1523/JNEUROSCI.0426-12.2013.

Martinez D, Arhidi L, Demondion E, Masson JB, Lucas P. Using Insect Electroantennogram Sensors on Autonomous Robots for Olfactory Searches. J Vis Exp. 2014 8; (90). doi: 10.3791/51704.

Martinez D, Chaffiol A, Voges N, Gu Y, Anton S, Rospars JP, Lucas P. Multiphasic On/Off Pheromone Signalling in Moths as Neural Correlates of a Search Strategy. PLoS ONE. 2013 4; 8(4):e61220. doi: 10.1371/journal.pone.0061220.

Mayer MS, Mankin RW. A new *Trichoplusia ni* antennal receptor neuron that responds to attomolar concentrations of a minor pheromone component. Experientia. 1990 3; 46(3):257–259. doi: 10.1007/BF01951757.

Montagné N, Chertemps T, Brigaud I, François A, François MC, de Fouchier A, Lucas P, Larsson MC, Jacquin-Joly E. Functional characterization of a sex pheromone receptor in the pest moth *Spodoptera littoralis* by heterologous expression in *Drosophila*. Eur J Neurosci. 2012 9; 36(5). doi: 10.1111/j.1460-9568.2012.08183.x.

Mukunda L, Miazzi F, Sargsyan V, Hansson BS, Wicher D. Calmodulin Affects Sensitization of *Drosophila melanogaster* Odorant Receptors. Front Cell Neurosci. 2016 2; 10. doi: 10.3389/fncel.2016.00028.

Murlis J, Willis MA, Cardé RT. Spatial and temporal structures of pheromone plumes in fields and forests. Physiol Entomol. 2000 9; 25(3):211–222. doi: 10.1046/j.1365-3032.2000.00176.x.

Nagel KI, Wilson RI. Biophysical mechanisms underlying olfactory receptor neuron dynamics. Nat Neurosci. 2011 2; 14(2):208–216. doi: 10.1038/nn.2725.

Olsson AM, Jönsson JA, Thelin B, Liljefors T. Determination of the vapor pressures of moth sex pheromone components by a gas chromatographic method. J Chem Ecol. 1983 3; 9(3). doi: 10.1007/BF00988456.

Pedregosa F, Varoquaux G, Gramfort A, Michel V, Thirion B, Grisel O, Blondel M, Prettenhofer P, Weiss R, Dubourg V, Vanderplas J, Passos A, Cournapeau D, Brucher M, Perrot M, Duchesnay E. Scikit-learn: Machine Learning in Python. J Mach Learn Res. 2011; 12:2825–2830.

Pézier A, Acquistapace A, Renou M, Rospars JP, Lucas P. Ca^{2+} Stabilizes the Membrane Potential of Moth Olfactory Receptor Neurons at Rest and Is Essential for Their Fast Repolarization. Chem Senses. 2007 5; 32(4). doi: 10.1093/chemse/bjl059.

Platkiewicz J, Brette R. A Threshold Equation for Action Potential Initiation. PLoS Comput Biol. 2010 7; 6(7):e1000850. doi: 10.1371/journal.pcbi.1000850.

Platkiewicz J, Brette R. Impact of Fast Sodium Channel Inactivation on Spike Threshold Dynamics and Synaptic Integration. PLoS Comput Biol. 2011 5; 7(5):e1001129. https://dx.plos.org/10.1371/journal.pcbi.1001129, doi: 10.1371/journal.pcbi.1001129.

Riffell JA, Shlizerman E, Sanders E, Abrell L, Medina B, Hinterwirth AJ, Kutz JN. Flower discrimination by pollinators in a dynamic chemical environment. Science. 2014 6; 344(6191):1515–1518. doi: 10.1126/science.1251041.

Rospars JP, Grémiaux A, Jarriault D, Chaffiol A, Monsempès C, Deisig N, Anton S, Lucas P, Martinez D. Heterogeneity and Convergence of Olfactory First-Order Neurons Account for the High Speed and Sensitivity of Second-Order Neurons. PLoS Comput Biol. 2014 12; 10(12):e1003975. doi: 10.1371/journal.pcbi.1003975.

Sane SP, Dieudonné A, Willis MA, Daniel TL. Antennal Mechanosensors Mediate Flight Control in Moths. Science. 2007 2; 315(5813):863–866. doi: 10.1126/science.1133598.

Sarno N, Hernandez-Clavijo A, Boccaccio A, Menini A, Pifferi S. Slow Inactivation of Sodium Channels Contributes to Short-Term Adaptation in Vomeronasal Sensory Neurons. eNeuro. 2022 5; 9(3):0471–21. doi: 10.1523/ENEURO.0471-21.2022.

Shorey HH. Animal communication by pheromones. Academic press; 1976.

Si G, Kanwal JK, Hu Y, Tabone CJ, Baron J, Berck M, Vignoud G, Samuel ADT. Structured Odorant Response Patterns across a Complete Olfactory Receptor Neuron Population. Neuron. 2019 3; 101(5):950–962. doi: 10.1016/j.neuron.2018.12.030.

Stimberg M, Brette R, Goodman DF. Brian 2, an intuitive and efficient neural simulator. eLife. 2019 8; 8. doi: 10.7554/eLife.47314.

Tiraboschi E, Leonardelli L, Segata G, Haase A. Parallel Processing of Olfactory and Mechanosensory Information in the Honey Bee Antennal Lobe. Front Physiol. 2021 12; 12. doi: 10.3389/fphys.2021.790453.

Tuckman H, Kim J, Rangan A, Lei H, Patel M. Dynamics of sensory integration of olfactory and mechanical stimuli within the response patterns of moth antennal lobe neurons. J Theor Biol. 2021 1; 509. doi: 10.1016/j.jtbi.2020.110510.

Tuckman H, Patel M, Lei H. Effects of Mechanosensory Input on the Tracking of Pulsatile Odor Stimuli by Moth Antennal Lobe Neurons. Front Neurosci. 2021 10; 15. doi: 10.3389/fnins.2021.739730.

Vetter RS, Sage AE, Justus KA, Cardé RT, Galizia CG. Temporal Integrity of an Airborne Odor Stimulus is Greatly Affected by Physical Aspects of the Odor Delivery System. Chem Sens. 2006 5; 31(4). doi: 10.1093/chemse/bjj040.

Vickers NJ, Baker TC. Reiterative responses to single strands of odor promote sustained upwind flight and odor source location by moths. Proc Natl Acad Sci USA. 1994 6; 91(13):5756–5760. doi: 10.1073/pnas.91.13.5756.

Vickers NJ. Winging It: Moth Flight Behavior and Responses of Olfactory Neurons Are Shaped by Pheromone Plume Dynamics. Chem Senses. 2006 2; 31(2):155–166. doi: 10.1093/chemse/bjj011.

Virtanen P, Gommers R, Oliphant TE, Haberland M, Reddy T, Cournapeau D, Burovski E, Peterson P, Weckesser W, Bright J, van der Walt SJ, Brett M, Wilson J, Millman KJ, Mayorov N, Nelson ARJ, Jones E, Kern R, Larson E, Carey CJ, et al. SciPy 1.0: fundamental algorithms for scientific computing in Python. Nat Methods. 2020 3; 17(3). doi: 10.1038/s41592-019-0686-2.

Wall C, Perry JN. Range of action of moth sex-attractant sources. Entomol Exp Appl. 1987 6; 44(1):5–14. doi: 10.1111/j.1570-7458.1987.tb02232.x.

Wang L, Nomura Y, Du Y, Dong K. Differential Effects of TipE and a TipE-Homologous Protein on Modulation of Gating Properties of Sodium Channels from *Drosophila melanogaster*. PLoS One. 2013 7; 8(7). doi: 10.1371/journal.pone.0067551.

Wicher D. Tuning insect odorant receptors. Frontiers in Cellular Neuroscience. 2018 4; 12:94. doi: 10.3389/FNCEL.2018.00094/BIBTEX.

Willis MA, Baker TC. Effects of intermittent and continuous pheromone stimulation on the flight behaviour of the oriental fruit moth, *Grapholita molesta*. Physiol Entomol. 1984 9; 9(3):341–358. doi: 10.1111/j.1365-3032.1984.tb00715.x.

Willis MA, Ford EA, Avondet JL. Odor tracking flight of male *Manduca sexta* moths along plumes of different cross-sectional area. J Comp Physiol A. 2013 11; 199(11):1015–1036. doi: 10.1007/s00359-013-0856-0.

Wilson RI. Early Olfactory Processing in *Drosophila* : Mechanisms and Principles. Annu Rev Neurosci. 2013 7; 36(1):217–241. doi: 10.1146/annurev-neuro-062111-150533.

Witzgall P, Kirsch P, Cork A. Sex Pheromones and Their Impact on Pest Management. J Chem Ecol. 2010 1; 36(1):80–100. doi: 10.1007/s10886-009-9737-y.

Zufall F, Stengl M, Franke C, Hildebrand J, Hatt H. Ionic currents of cultured olfactory receptor neurons from antennae of male *Manduca sexta*. J Neurosci. 1991 4; 11(4):956–965. doi: 10.1523/JNEUROSCI.11-04-00956.1991.

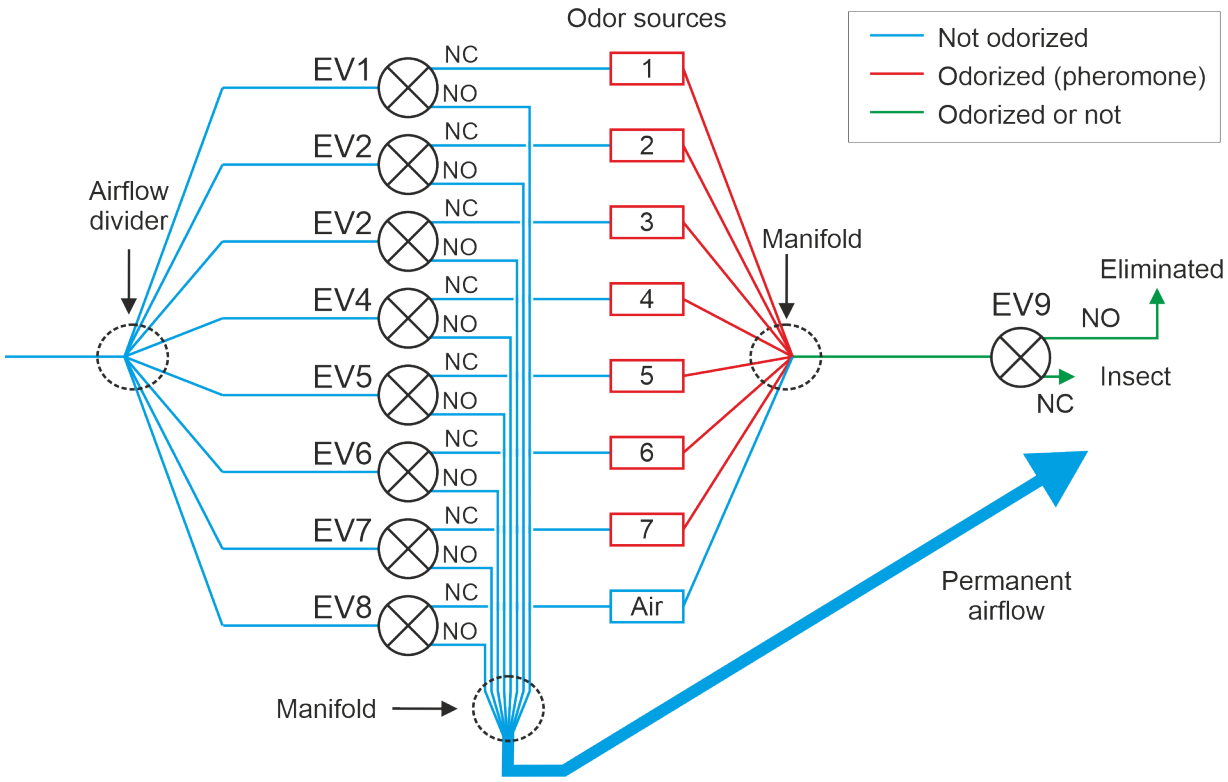

Figure 1–Figure supplement 1. NO: normally open (no stimulus) and NC normally closed (during stimulus). The insect is placed 1 mm after EV9.

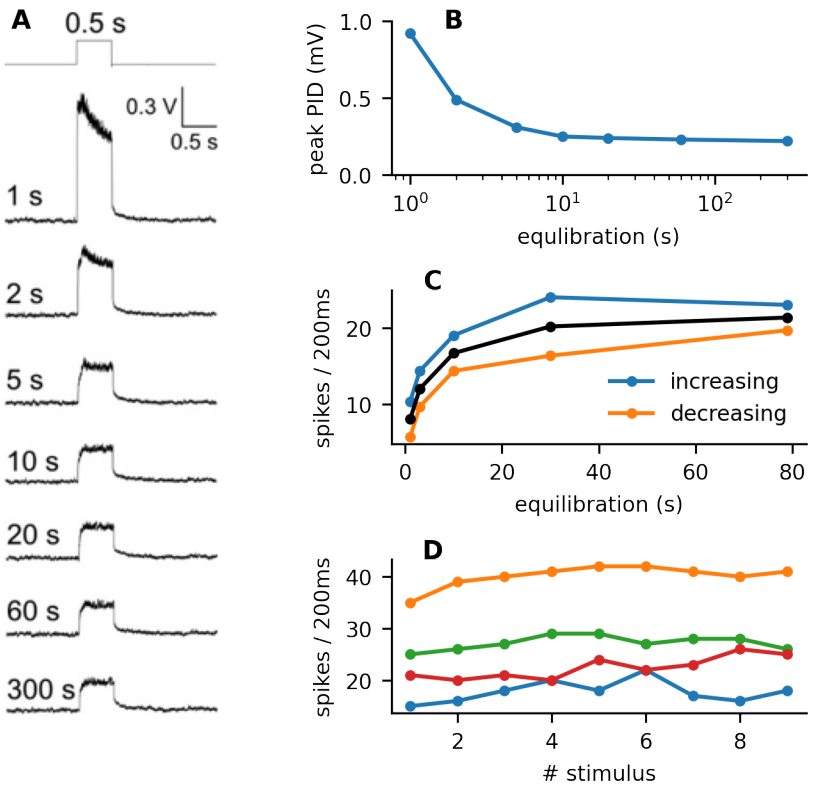

Figure 1–Figure supplement 2. A: Traces of PID recordings of linalool with different equilibration times. When the equilibration is too short, the PID response exhibits a transient peak. **B:** With an equilibration of approximately 10 s the peak is no longer present and the amplitude of the response does not change significantly with longer equilibration times. **C:** Number of spikes recorded in 200 ms in response to 100 pg of Z7-12:Ac for different equilibration times. Each ORN was presented with 5 stimuli with different equilibration times (1 s, 3 s, 10 s, 30 s, 79 s) either in increasing or decreasing order. For each order, the line is an average of 3 ORNs. The black line is an average of all 6 ORNs. **D:** We measured the stability of the pheromone source first by applying 9 stimuli with 0.1 ng of Z7-12:Ac. Each stimulus was preceded by an equilibration time of 30 s. The inter stimulus interval was 2 min. Each line represents the response of a single ORN.

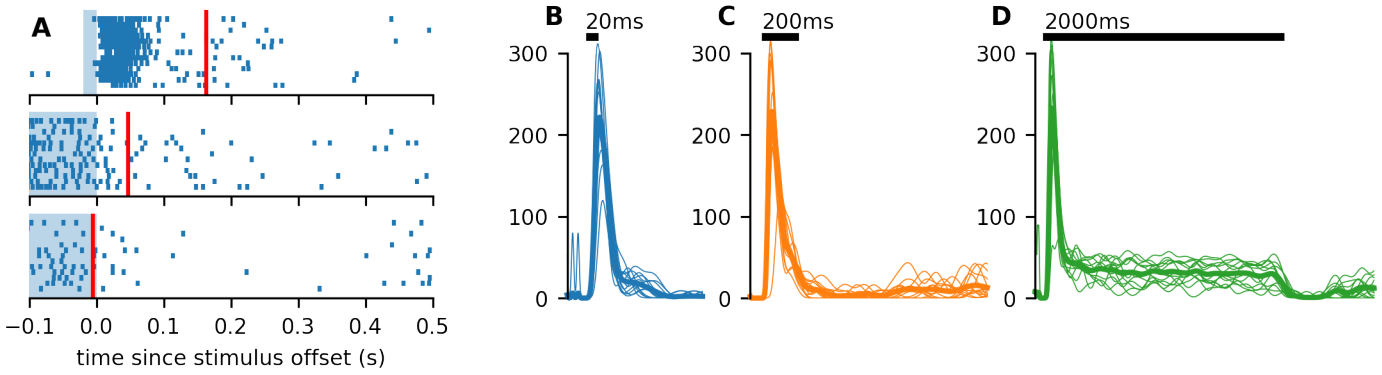

Figure 2–Figure supplement 1. A: Raster plots of *Spodoptera littoralis* ORN responses to different stimulus durations, aligned to the stimulus offset, show that the response pattern to stimuli of different durations remains unchanged. ORNs exhibit a prolonged response to short stimuli and transient inhibition shortly after offset of long stimuli. **B-D:** Full firing profiles of responses to different stimulus durations.

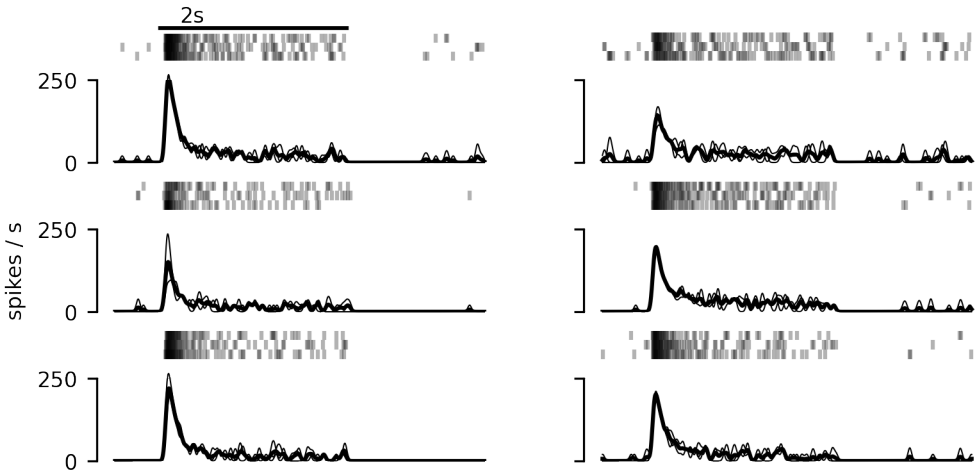

Figure 2–Figure supplement 2. To avoid mechanical artefacts during odor stimuli, we added a second electrovalve to deliver non-odorized air. This valve was in opposing phase with the valve that delivers odor stimuli so that the airflow sent to the antenna was constant before, during and after stimuli. We still observed the inhibitory phase after the stimulus offset, indicating that it is not a mechanical artefact.

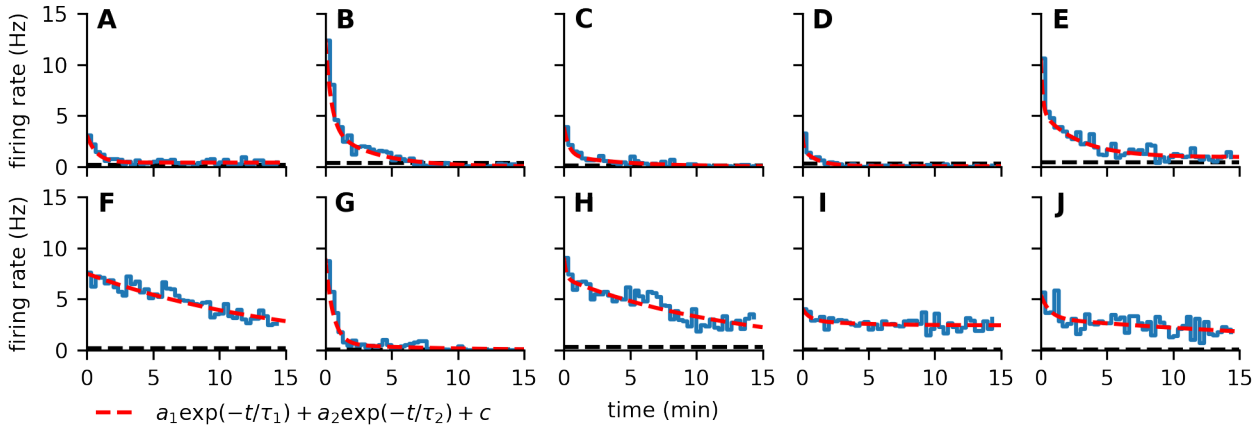

dose 10 pg

	a_1	τ_1	a_2	τ_2	c	spont.
A	2.69	43.66	0.00	43.3	0.39	0.18
B	8.66	25.96	3.83	202.0	0.00	0.36
C	2.76	23.24	1.12	266.6	0.00	0.13
D	1.51	5.52	1.70	67.5	0.04	0.27
E	5.16	8.53	4.52	169.1	0.93	0.44

dose 1 ng

	a_1	τ_1	a_2	τ_2	c	spont.
F	0.09	0.83	7.51	927.1	0.00	0.16
G	8.36	34.58	0.63	462.4	0.00	0.03
H	2.02	10.45	7.04	789.6	0.00	0.31
I	1.12	32.05	0.52	233.8	2.43	0.09
J	2.27	39.85	3.14	1672.8	0.00	0.09

Figure 2–Figure supplement 3. We first measured the spontaneous activity during a 15 min period (black dashed lines) and then stimulated the ORN with either 10 pg (**A-E**) or 1 ng (**F-J**) dose of pheromone. Blue lines indicate the firing rate as measured by counting spikes in 20 s bins, starting 3 s after the pulse offset. Red dashed lines show a double exponential fit. The ORNs stimulated with a 1 ng did not return close to their spontaneous activity within the 15 min period (except for **G**). The fitter parameters are provided in the tables.

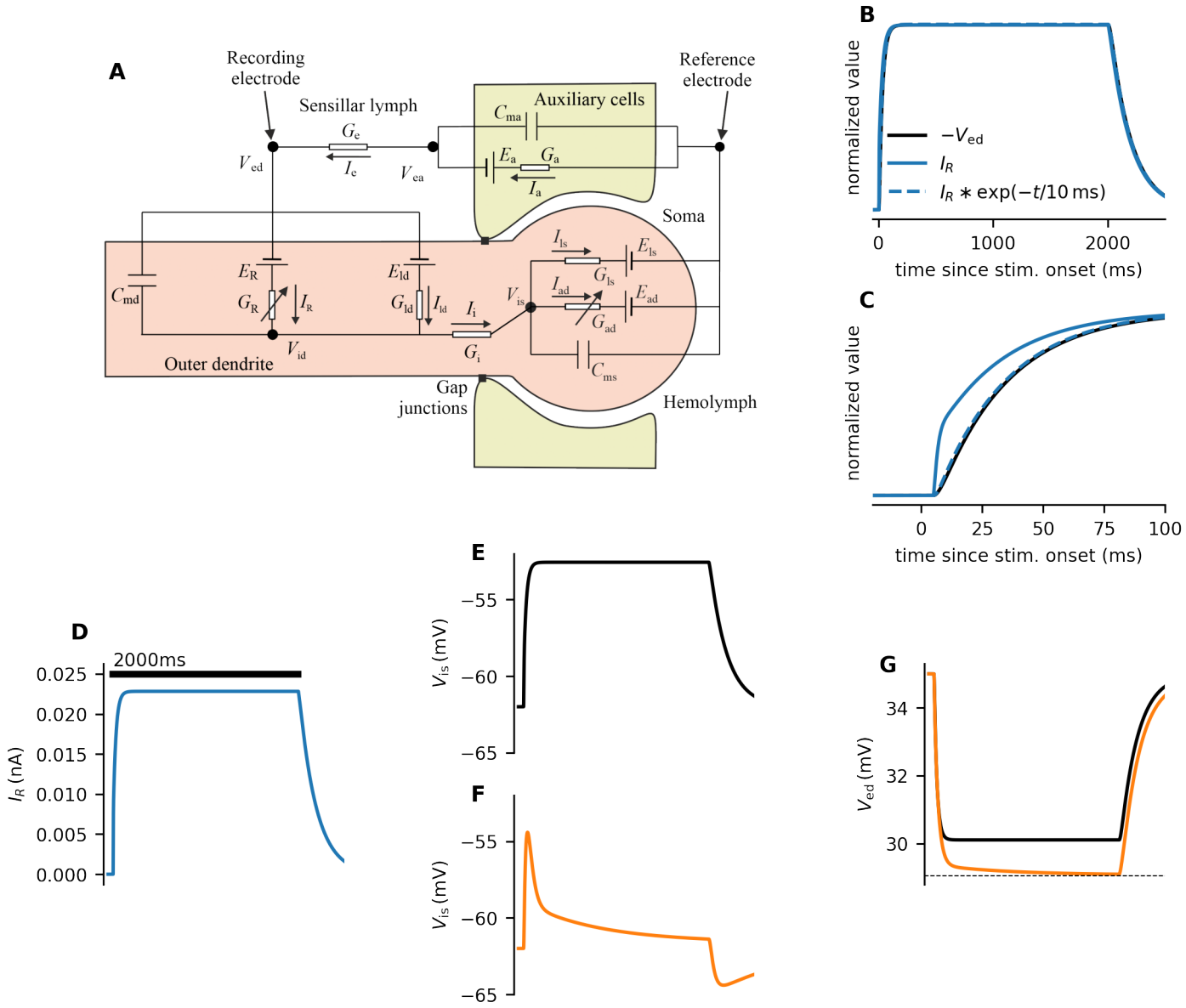

Figure 4–Figure supplement 1. A: A: Schematic illustration of the model. See Materials and methods for details. **B-C:** LFP (V_{ed}) and the corresponding estimated receptor current I_R (normalized, LFP changed from negative to positive). Dashed is the receptor current smoothed with an exponential filter: $I_R * \exp(-t/10\,\mathrm{ms})$. **D:** The input current from **C**, used as an input the model can lead to different time course of the somatic membrane potential (V_{is}), depending on the adaptation currents in the soma (**E-F**). In **E**, no adaptation current is involved ($I_{ad} = 0$). In **F**, the adaptation current is calculated so that the somatic membrane potential resembles the firing rate of the ORN. The adaptation current then changes the time course of the LFP (**G**).

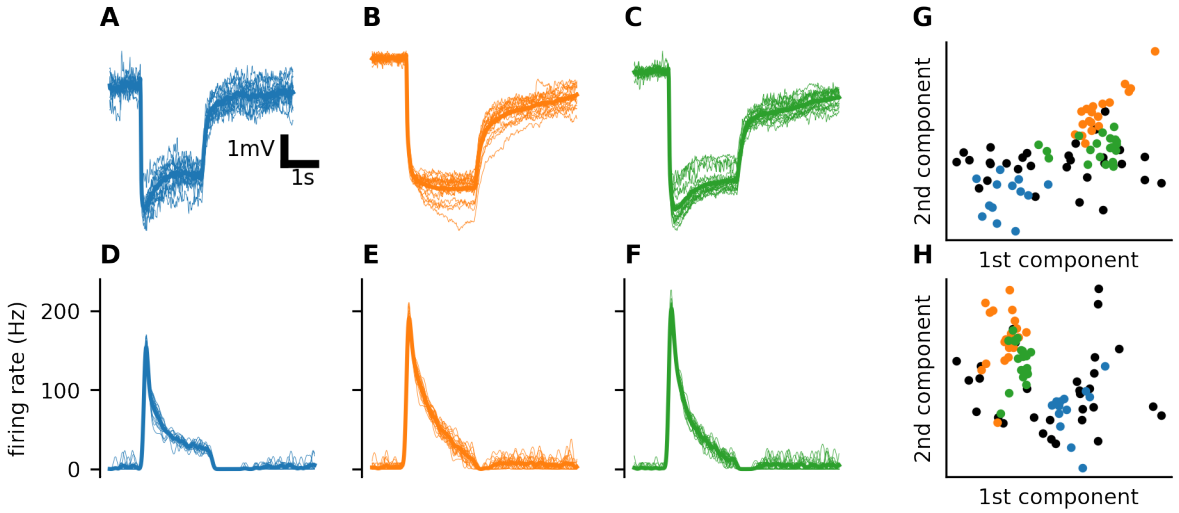

Figure 4–Figure supplement 2. A-C: LFP in response to a 2 s stimulus. Each panel (color) corresponds to a single neuron presented several times with the same stimulus. Thin lines are the individual trials, the thick line represents their average. **D-F:** Firing profiles of the three different neurons. Colors represent the neuron, as in **A-C**. Thin lines are the individual trials, the thick line represents their average. **G:** Scatter plot of the first two PCA components of the LFP. Each black point corresponds to a different neuron, while each of the colored points represents a single trial of one of the three neurons from **A-C**. The colored points are always concentrating around one spot, indicating that the responses of each neurons are stable in time and do not capture the heterogeneity of the whole population. **H:** Same as **G**, but for the firing rate profiles.

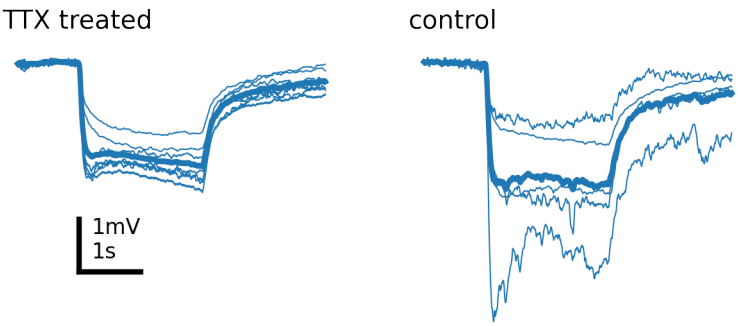

Figure 4–Figure supplement 3. The TTX treated ORNs ($N = 7$) exhibited similar LFP response shape as the control ORNs ($N = 5$), including a peak in deflection towards the end of the stimulus, indicating that this slow deflection is not caused by the spiking activity.

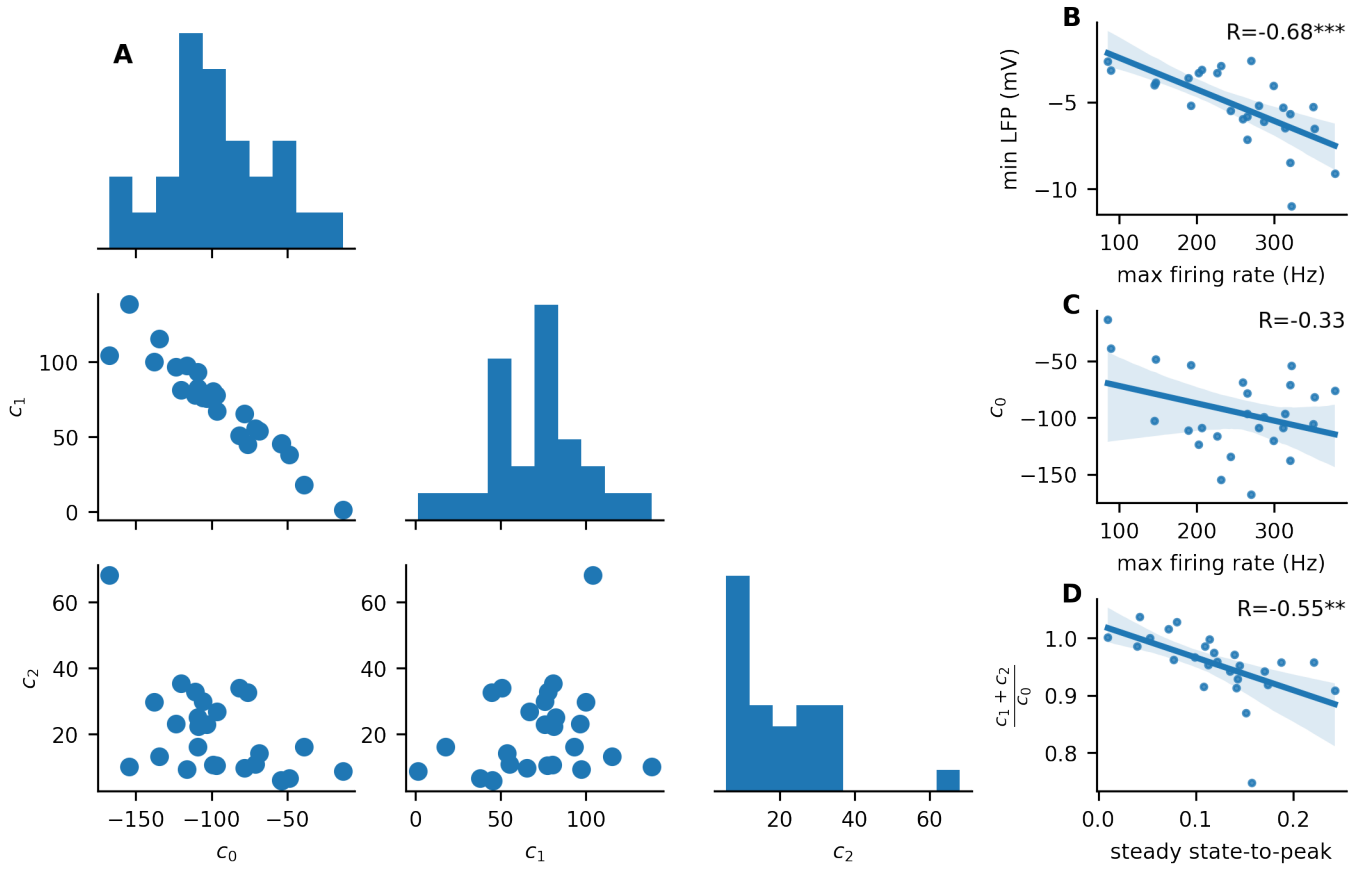

Figure 5–Figure supplement 1. A: Distributions of filter coefficients c_0, c_1 and c_2 and their mutual dependence. While c_0 and c_1 are tightly correlated, c_2, responsible for the slow adaptation is rather independent. **B:** Higher amplitudes of initial LFP deflection (min. LFP during 200 ms stimulus) is correlated (Pearson correlation, $p = 1.5 \cdot 10^{-4}$) with the peak firing rate of the neuron (calculated with $\mathrm{bw} = 30\,\mathrm{ms}$). **C:** We did not see a significant correlation between the peak firing rate and c_0 (Pearson correlation, $p = 0.097$). **D:** We saw a significant correlation (Pearson correlation, $p = 3.9 \cdot 10^{-3}$) between the steady state-to-peak ratio (ratio of the mean firing rate in the last 0.5 s of 2 s stimulus to the peak firing rate).

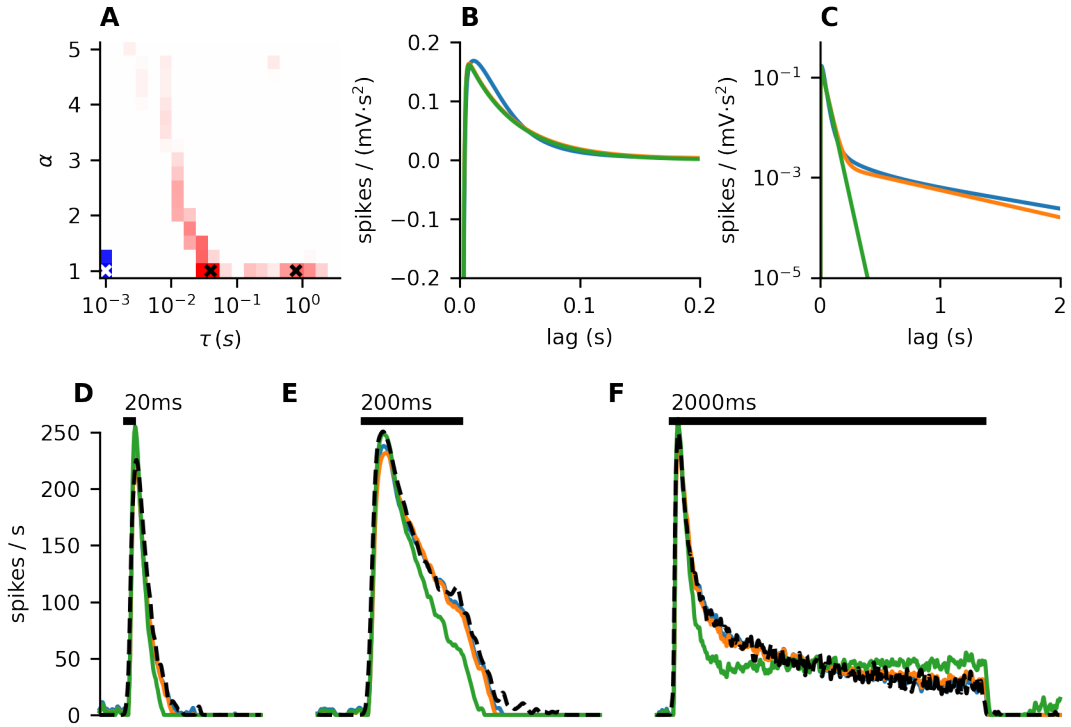

Figure 5–Figure supplement 2. **A:** heatmap of lasso regression coefficient values for different time constants τ and gamma distribution shapes α. Blue indicates a negative value, red positive value and white is zero. The non-zero values concentrate around several spots. Based on this analysis, we selected the time constants 1 ms, 40 ms and 800 ms, which are marked by crosses in the heatmap. **B:** Three different linear filters: filter corresponding to the lasso regression, filter obtained from linear regression with the three exponential kernels with the time constants 1 ms, 40 ms, 800 ms and filter obtained from linear regression with only two exponential kernels (1 ms and 40 ms). Note the difference with **Figure 5**E, where the filter with two kernels is obtained by fitting a filter with three kernels and only then removing the slow component. **C:** The same filters as in **B**, but on logarithmic scale to accent the differences between individual filters. **D-F:** Predictions of firing responses with the linear filters from **B**, color-coded accordingly. Note that even though the filters with three exponential kernels and the filter obtained from the lasso regression are obviously different, their predictions are almost identical.

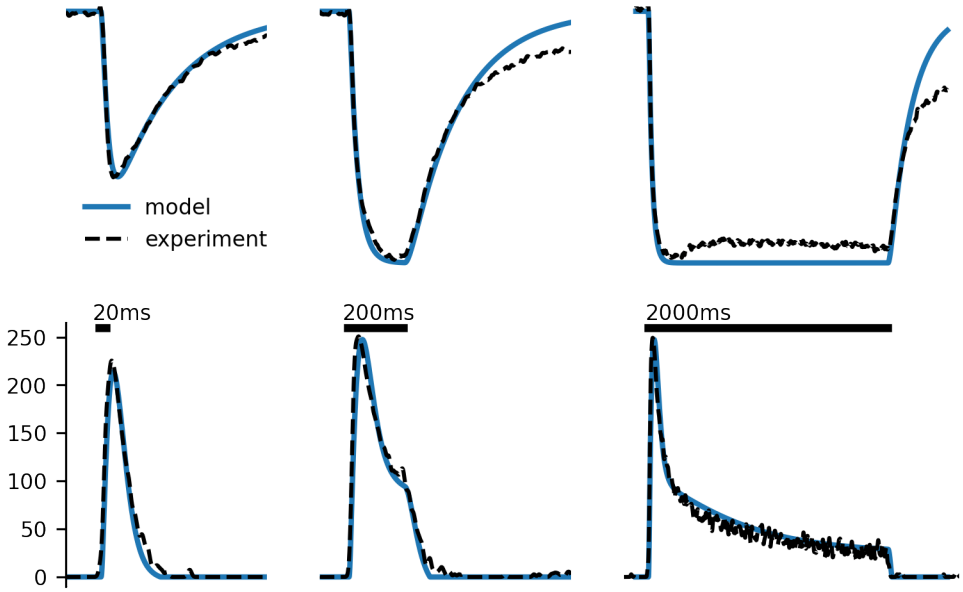

Figure 5–Figure supplement 3. Prediction of LFP (top row) and firing rate (bottom row) using an odor transduction model (**Equation 4-Equation 5**) combined with the linear-nonlinear model (**Equation 1-Equation 2**). The transduction model was fit to the average LFP (first 400 ms of the 20 ms and 200 ms stimuli) and the LN model was fit to transform the average LFP to the average firing rate (2 s stimulus) (indicated by the dashed lines). Note that the model neglects receptor adaptation and the sustained activity.

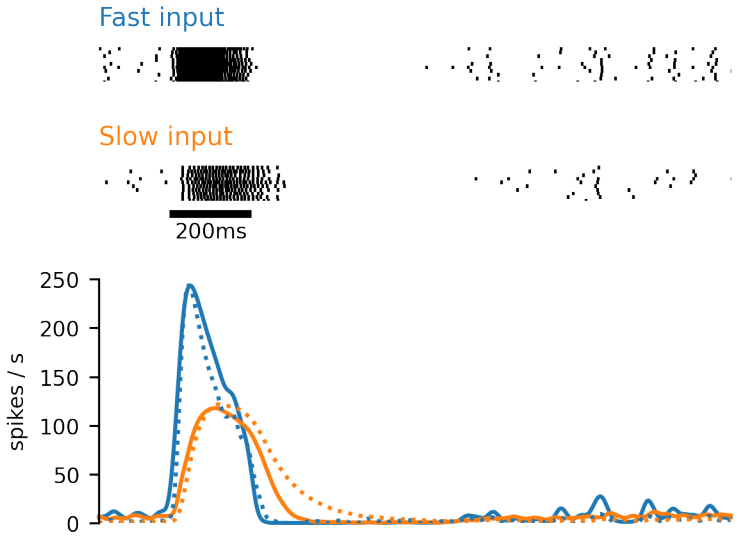

Figure 6–Figure supplement 1. The raster plots at the top show the spike trains of the 10 PNs in response to the unmodified ORN firing profile (Fast input) and ORN firing profile smoothed with exponential kernel with 100 ms mean (Slow input). The PNs with the slow input also exhibit the inhibitory phase, but do not track the stimulus duration. The full lines in the bottom panel show the PN firing rate averaged over 36 simulations. The dotted lines show the ORN input.